Two-resonator circuit quantum electrodynamics: A superconducting quantum switch

Matteo Mariantoni,[1,2,*] Frank Deppe,[1,2,†] A. Marx,[1] R. Gross,[1,2] F. K. Wilhelm,[3] and E. Solano[4,5]
[1]*Walther-Meißner-Institut, Bayerische Akademie der Wissenschaften, Walther-Meißner-Strasse 8, D-85748 Garching, Germany*
[2]*Physics Department, Technische Universität München, D-85748 Garching, Germany*
[3]*Institute for Quantum Computing and Department of Physics and Astronomy, University of Waterloo, 200 University Avenue West, Waterloo, Ontario, Canada N2L 3G1*
[4]*Physics Department, CeNS, and ASC, Ludwig-Maximilians-Universität, Theresienstrasse 37, D-80333 Munich, Germany*
[5]*Departamento de Química Física, Universidad del País Vasco–Euskal Herriko Unibertsitatea, Apartado 644, 48080 Bilbao, Spain*
(Received 14 February 2008; revised manuscript received 13 August 2008; published 11 September 2008)

We introduce a systematic formalism for two-resonator circuit QED, where two on-chip microwave resonators are simultaneously coupled to one superconducting qubit. Within this framework, we demonstrate that the qubit can function as a quantum switch between the two resonators, which are assumed to be originally independent. In this three-circuit network, the qubit mediates a *geometric second-order circuit interaction* between the otherwise decoupled resonators. In the dispersive regime, it also gives rise to a *dynamic second-order perturbative interaction*. The geometric and dynamic coupling strengths can be tuned to be equal, thus permitting to switch on and off the interaction between the two resonators via a qubit population inversion or a shifting of the qubit operation point. We also show that our quantum switch represents a flexible architecture for the manipulation and generation of nonclassical microwave field states as well as the creation of controlled multipartite entanglement in circuit QED. In addition, we clarify the role played by the geometric interaction, which constitutes a fundamental property characteristic of superconducting quantum circuits without a counterpart in quantum-optical systems. We develop a detailed theory of the geometric second-order coupling by means of circuit transformations for superconducting charge and flux qubits. Furthermore, we show the robustness of the quantum switch operation with respect to decoherence mechanisms. Finally, we propose a realistic design for a two-resonator circuit QED setup based on a flux qubit and estimate all the related parameters. In this manner, we show that this setup can be used to implement a superconducting quantum switch with available technology.

DOI: 10.1103/PhysRevB.78.104508 PACS number(s): 84.30.Bv, 03.67.Lx, 32.60.+i, 42.50.Pq

I. INTRODUCTION

In the past few years, we have witnessed a tremendous experimental progress in the flourishing realm of circuit QED.[1–4] Different types of superconducting qubits have been strongly coupled to on-chip microwave resonators, which act as quantized cavities. Recently, a quantum state has been stored and coherently transferred between two superconducting phase qubits via a microwave resonator[5] and two transmon qubits have been coupled utilizing an on-chip cavity as a quantum bus.[6] Furthermore, microwave single photons have been generated by spontaneous emission[7] and Fock states created in a system based on a phase qubit.[8] In addition, lasing effects have been demonstrated exploiting a single Cooper-pair box,[9] the nonlinear response of the Jaynes-Cummings (JC) model has been observed,[10,11] the two-photon driven JC dynamics has been used as a means to probe the symmetry properties of a flux qubit,[12] and resonators have been tuned with high fidelity.[13,14] These formidable advances show how circuit QED systems are rapidly reaching a level of complexity comparable to that of the already well-established quantum-optical cavity QED.[15–17]

Among the aims common to these experiments is the possibility of performing quantum information processing,[18] in particular following the lines of recent proposals; e.g., see Refs. 19 and 20. The latter considered a two-dimensional array of on-chip resonators coupled to qubits. In this or any other multicavity setup,[21] it is highly desirable to switch on and off an interaction between two resonators or to compensate for their spurious cross-talk. Moreover, investigating the basic properties of two-resonator circuit QED, where two resonators are coupled to one qubit, certainly represents a subject of fundamental relevance. In fact, when operating such a system in a regime dominated by second-order (dispersive) interactions, as in the scope of this paper, the requirements on the qubit coherence properties are considerably relaxed.[22,23] In this manner, two-resonator architectures constitute an appealing playground for testing quantum mechanics on a chip. We also notice that second-order interactions[12,24] are becoming more and more prominent in circuit QED experiments owing to the possibility of very large first-order coupling strengths.[3–12,24,25]

In this paper, we theoretically study a three-circuit network where a superconducting charge or flux qubit[26–29] interacts with two on-chip microwave cavities, a two-resonator circuit QED setup. In the absence of the qubit, the resonators are assumed to have negligible or small geometric first-order (direct) cross-talk. This scenario is similar to that of quantum optics, where an atom can interact with two orthogonal-cavity modes.[30] However, there are some crucial differences. The nature of the three-circuit system considered here requires accounting for a *geometric second-order circuit interaction* between the two resonators. This gives rise to coupling terms in the interaction Hamiltonian, which are formally equivalent to those describing a beam splitter. This interaction is mediated by the circuit part of the qubit and does not depend on the qubit state. It is worth mentioning

that this coupling does not exist in the two-mode JC model studied in quantum optics, where atoms do not sustain any geometric interaction. This means that introducing a second resonator causes a departure from the neat analogy between cavity and one-resonator circuit QED.[22,31–34] In the dispersive regime, where the transition frequency of the qubit is largely detuned from that of the cavities, other beam-splitter-type interaction terms between the two resonators also appear. Their existence is known in quantum optics[35] and results from a *dynamic second-order perturbative interaction*, which depends on the state of the qubit. The sign of this interaction can be changed by an inversion of the qubit population or by shifting of the qubit operation point. The latter mechanism can also be used to change the interaction strength. Notably, for a suitable set of parameters, the geometric and dynamic second-order coupling coefficients can be made exactly equal by choosing a proper qubit-resonator detuning. In this case, the interaction between the two cavities can be switched on and off, thereby enabling the implementation of a *discrete quantum switch* as well as a *tunable coupler*.

In circuit QED, several other scenarios have been envisioned where a qubit interacts with different bosonic modes, e.g., those of an adjacent nanomechanical resonator or similar. It has been proposed to implement quantum transducers[36] as well as Jahn-Teller models and Kerr nonlinearities,[37] to generate nontrivial nonclassical states of the microwave radiation,[21,38] to create entanglement via Landau-Zener sweeps,[39] and to carry out high fidelity measurements of microwave quantum fields.[38,40] Moreover, multiresonator setups might serve in probing quantum walks[41] and studying the scattering process of single microwave photons.[42] All of these proposals, however, do not develop a systematic theory of a realistic architecture based on two on-chip microwave resonators and do not take into account the fundamental geometric second-order coupling between them. Also, our quantum switch is inherently different from the quantum switches investigated in atomic systems.[43] First, we consider a qubit simultaneously coupled to two resonators, which are not positioned one after the other in a cascade configuration as in Ref. 43. Second, our switch behaves as a tunable quantum coupler between the two resonators. Last, atomic systems naturally lack a geometric second-order coupling. Furthermore, it is important to stress that the dynamic interaction studied here cannot be cast within the framework of the quantum reactance theory (capacitance or inductance, depending on the specific implementation).[44–51] The main hypothesis for a quantum reactance to be defined is a resonator characterized by a transition frequency extremely different from that of the qubit. Typically, the resonator frequency is considered to be very low (practically zero) compared to the qubit one. Such a scenario is undesirable for the purposes of this work, where a truly quantized high-frequency cavity initialized in the vacuum state has to be used. Also, to our knowledge, the quantum reactance works mentioned above do not directly exploit a geometric coupling between two resonators to compensate for a dynamic one. Nevertheless, we believe that a circuit theory approach[27,52–57] to two-resonator circuit QED, which we pursue throughout this paper, allows for a deep comprehension of the matter discussed here. Finally, we point out that the geometric first-order coupling between two resonators can be reduced or erased by simple engineering, whereas the second-order coupling due to the presence of a qubit circuit is a fundamental issue. As we show later, whenever we want the coupling between qubit and resonators to be large, an appreciable geometric second-order coupling inevitably appears, especially for resonators perfectly isolated in first order. In summary, our quantum switch is based on a combination of geometric and dynamic interactions competing against each other and is a promising candidate to perform nontrivial quantum operations between different resonators.

The paper is organized as follows: In Sec. II, we develop a systematic formalism for two-resonator circuit QED employing second-order circuit theory. In Sec. III, we focus on the dispersive regime of two-resonator circuit QED and derive the quantum switch Hamiltonian. In Sec. IV, we discuss the main limitations to the quantum switch operation due to decoherence processes of qubit and cavities. In Sec. V, we propose a realistic implementation of a two-resonator circuit QED architecture, which is suitable for the realization of a superconducting quantum switch. Finally, in Sec. VI, we summarize our main results, draw our conclusions, and give a brief outlook.

II. TWO-RESONATOR CIRCUIT QED

In this section, we take the perspective of classical circuit theory[57] and extend it to the quantum regime to derive the Hamiltonian of a quantized three-circuit network. In general, the latter is composed of two on-chip microwave resonators and a superconducting qubit. Our approach is similar to that of Refs. 27 and 52–56. In addition, we account for second-order circuit elements linking different parts of the network, which is considered to be closed and nondissipative. Here, closed means that we assume no energy flow between the network under analysis and other possible adjacent networks. These could be additional circuitry used to access the three-circuit network from outside and where excitations could possibly decay. Nondissipative means that we consider capacitive and inductive circuit elements only, or in general, reactive elements. We neglect resistors, which could represent dissipation processes of qubit and resonators. In summary, the network of our model is altogether a conservative system. The detailed role of decoherence mechanisms is studied later in Sec. IV.

The first step of our derivation is to demonstrate a geometric second-order coupling between the circuit elements of a simple *three-node network*. This means that we assume the various circuit elements to be concentrated in three confined regions of space (nodes). Any topologically complex *three-circuit network* can be reduced to such a three-node network, where each node is fully characterized by its capacitance matrix **C** and/or inductance matrix **M**. The topology of the different circuits (e.g., two microstrip or coplanar waveguide resonators coupled to a superconducting qubit) is thus absorbed in the definition of **C** and **M**, simplifying the analysis significantly. The system Hamiltonian can then be straightforwardly obtained. In fact, the classical energy of a conser-

vative network can be expressed as $E=(\vec{V}^T\mathbf{C}\vec{V}+\vec{I}^T\mathbf{M}\vec{I})/2$, where the vectors $\vec{V}$ and $\vec{I}$ represent the voltages and currents on the various capacitors and inductors.[57] The usual quantization of voltages and currents[22] and the addition of the qubit Hamiltonian allows us to obtain the fully quantized Hamiltonian of the three-node network (cf. Sec. II A). Special attention is then reserved to compute contributions to the matrices $\mathbf{C}$ and $\mathbf{M}$ up to second order. These are consequently redefined as $\mathbf{C}^{(2)}$ and $\mathbf{M}^{(2)}$, respectively (cf. Sec. II B). Corrections of third or higher order to the capacitance and inductance matrices are discussed in Appendix A, where we show that they are not relevant for this work.

We finally consider two examples of possible implementations of two-resonator circuit QED (cf. Sec. II C). These examples account for two superconducting resonators coupled to a charge quantum circuit (e.g., a Cooper-pair box or a transmon) or a flux quantum circuit (e.g., a superconducting one- or three-Josephson-junction loop). Before moving to a two-level approximation, the Hamiltonians of these devices can be used to deduce the geometric second-order circuit interaction between the two resonators. This result is better understood considering the lumped-element equivalent circuits of the entire systems. In this way, the conceptual step from a three-circuit to a three-node network is also clarified and the role played by the topology of the different circuits becomes more evident. We show that special care must be taken when quantizing the interaction Hamiltonian between charge or flux quantum circuits and microwave fields by the simple promotion of an ac classical field to a quantum one. Interestingly, comparing the standard Hamiltonian of charge and flux quantum circuits coupled to quantized fields with *ab initio* models based on lumped-element equivalent circuits, we prove that the latter are better suited to describe circuit QED systems.

A. Hamiltonian of a generic three-node network

The system to be studied is sketched in Figs. 1(a) and 1(b), where the microwave resonators are represented by symbolic mirrors. A more realistic setup is discussed in Sec. V and is drawn in Fig. 6(a). A and B represent the two cavities and Q represents a superconducting qubit, making altogether a three-node network. The coupling channels between the three nodes are assumed to be capacitive and/or inductive [for simplicity, in Figs. 1(a) and 1(b) only inductive couplings are considered]. We also hypothesize the first-order interaction between A and B to be weak and that between A or B and Q to be strong by design. In other words, the first-order capacitance and inductance matrices are $\mathbf{C}=C_{kl}$ and $\mathbf{M}=M_{kl}$, with $k,l\in\{\mathrm{A},\mathrm{B},\mathrm{Q}\}$, where $C_{kl}=C_{lk}$ and $M_{kl}=M_{lk}$ because of symmetry reasons. In addition, we assume $C_{\mathrm{AB}}\equiv c\ll C_{kl\neq\mathrm{AB}}$ and $M_{\mathrm{AB}}\equiv m\ll M_{kl\neq\mathrm{AB}}$. The elements c and m represent a first-order cross-talk between A and B, which can be either spurious or engineered and, here, is considered to be small. In Sec. V, we delve into a more detailed analysis of the geometric first-order coupling between two microstrip resonators. Restricting the cavities to a single relevant mode, the total Hamiltonian of the system is given by

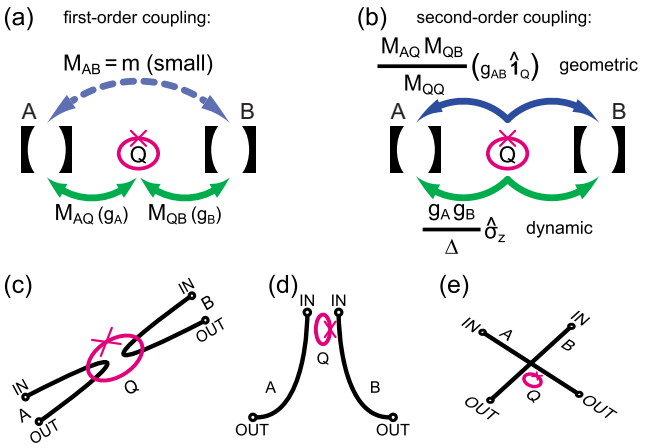

FIG. 1. (Color online) (a), (b) Sketches of the system under analysis. All constants are defined in the main body of the paper. Only inductive couplings are considered. (a) Schematic representation of the first-order coupling Hamiltonian of our three-node network. Two cavities (resonators) A and B interact with a generic superconducting qubit Q. A and B can have a weak geometric first-order coupling $\propto M_{\mathrm{AB}}=m$ [broken blue (dark gray) arrow], as in the Hamiltonian $\hat{H}^{(1)}_{\mathrm{AB}}$ in Eq. (2). The two solid green (light gray) arrows represent a two-mode Jaynes-Cummings dynamics with coupling coefficients $g_{\mathrm{A}}\propto M_{\mathrm{AQ}}$ and $g_{\mathrm{B}}\propto M_{\mathrm{QB}}$. (b) Visualization of the effective second-order coupling Hamiltonian $\hat{H}_{\mathrm{eff}}$ in Eq. (14). The solid blue (dark gray) arrows show the second-order *geometric* coupling channel mediated by a virtual excitation of the circuit associated with Q, as in the Hamiltonian $\hat{H}^{(2)}_{\mathrm{AB}}$ in Eq. (3). This channel is characterized by a coupling coefficient $g_{\mathrm{AB}}\propto M_{\mathrm{AQ}}M_{\mathrm{QB}}/M_{\mathrm{QQ}}$ (the small contribution from m is neglected) and is qubit-state independent. The solid green (light gray) arrows show the second-order *dynamic* channel mediated by a virtual excitation of the qubit Q. This channel is characterized by a coupling coefficient $\propto g_{\mathrm{A}}g_{\mathrm{B}}/\Delta$ and is qubit-state dependent. (c)-(e) Three generic sketches of a possible setup: (c) A flux qubit (Q) sits at the current antinode of, e.g., the first mode of two $\lambda/2$ resonators (solid black lines; only the inner conductor is shown). The open circles at the "IN" and "OUT" ports denote the position of the coupling capacitors to be used in real implementations [e.g., cf. Sec. V and Fig. 6(a)]. (d) A charge qubit (Q) sits at the voltage antinode of, e.g., the first mode of two $\lambda/2$ resonators. (e) A charge or flux qubit sits at the voltage (e.g., second mode, λ resonators) or current (e.g., first mode, $\lambda/2$ resonators) antinode, respectively, of two orthogonal resonators (Ref. 20).

$$\hat{H}_T=\frac{1}{2}\vec{\hat{V}}^T\mathbf{C}^{(\mathbf{n})}\vec{\hat{V}}+\frac{1}{2}\vec{\hat{I}}^T\mathbf{M}^{(\mathbf{n})}\vec{\hat{I}}+\frac{1}{2}G(E_c,E_J)\hat{\tilde{\sigma}}_x, \qquad (1)$$

where $\mathbf{C}^{(\mathbf{n})}$ and $\mathbf{M}^{(\mathbf{n})}$ are the renormalized capacitance and inductance matrices up to the nth order, with $\mathbf{C}^{(\mathbf{1})}\equiv\mathbf{C}$ and $\mathbf{M}^{(\mathbf{1})}\equiv\mathbf{M}$. Also, $\vec{\hat{V}}\equiv[\hat{V}_{\mathrm{A}},\hat{V}_{\mathrm{B}},\hat{V}_{\mathrm{Q}}]^T$ and $\vec{\hat{I}}\equiv[\hat{I}_{\mathrm{A}},\hat{I}_{\mathrm{B}},\hat{I}_{\mathrm{Q}}]^T$. In general, G is a function of the charging energy E_c and/or coupling energy E_J of the Josephson-tunnel junctions in the qubit. For instance, $G=E_J$ for a charge qubit and $G\propto\sqrt{E_cE_J}\exp(-\mu\sqrt{E_c/E_J})$ for a flux qubit ($\mu\equiv$const). Furthermore, $\hat{V}_{\mathrm{A}}\equiv v_{\mathrm{dc}}+v_{\mathrm{A0}}(\hat{a}^\dagger+\hat{a})$, $\hat{V}_{\mathrm{B}}\equiv v_{\mathrm{B0}}(\hat{b}^\dagger+\hat{b})$, $\hat{V}_{\mathrm{Q}}\equiv v_{\mathrm{Q}}\hat{\tilde{\sigma}}_z$, $\hat{I}_{\mathrm{A}}\equiv i_{\mathrm{dc}}+i_{\mathrm{A0}}j(\hat{a}^\dagger-\hat{a})$, $\hat{I}_{\mathrm{B}}\equiv i_{\mathrm{B0}}j(\hat{b}^\dagger-\hat{b})$, and $\hat{I}_{\mathrm{Q}}\equiv i_{\mathrm{Q}}\hat{\tilde{\sigma}}_z$. In these

expressions, $\hat{\tilde{\sigma}}_x$ and $\hat{\tilde{\sigma}}_z$ are the usual Pauli operators for a spin-1/2 system in the diabatic basis, which consists of the eigenstates $|-\rangle$ and $|+\rangle$ of $C_{\mathrm{AQ}}v_{\mathrm{dc}}v_{\mathrm{Q}}\hat{\tilde{\sigma}}_z$ (charge case) or $M_{\mathrm{AQ}}i_{\mathrm{dc}}i_{\mathrm{Q}}\hat{\tilde{\sigma}}_z$ (flux case). Additionally, $\hat{a}^\dagger$, $\hat{b}^\dagger$, $\hat{a}$, and $\hat{b}$ are bosonic creation and annihilation operators for the fields of cavities A and B, respectively, and $j\equiv\sqrt{-1}$. The dc voltage v_{dc} and current i_{dc} account for the quasistatic polarization of the qubit and can be applied through any suitable bias circuit. For definiteness, we have chosen here cavity A to perform this function. This is the standard approach followed by the charge qubit circuit QED community.[1] However, for flux qubits the current i_{dc} is more easily applied via an external coil.[3,12,25,58] In the latter case, we impose $i_{\mathrm{dc}}=0$ and add to the Hamiltonian in Eq. (1) the term $(\Phi_x^{\mathrm{dc}}-\Phi_0/2)\hat{I}_{\mathrm{Q}}$, where Φ_x^{dc} is an externally applied flux bias and $\Phi_0\equiv h/2e=2.07\times10^{-15}$ Wb is the flux quantum. The results of our derivation are not affected by this particular choice. The vacuum (zero-point) fluctuations in the voltage and current of each resonator are given by $v_{\mathrm{A0}}\equiv\sqrt{\hbar\omega_{\mathrm{A}}/2C_{\mathrm{AA}}}$ and $v_{\mathrm{B0}}\equiv\sqrt{\hbar\omega_{\mathrm{B}}/2C_{\mathrm{BB}}}$ and $i_{\mathrm{A0}}\equiv\sqrt{\hbar\omega_{\mathrm{A}}/2M_{\mathrm{AA}}}$ and $i_{\mathrm{B0}}\equiv\sqrt{\hbar\omega_{\mathrm{B}}/2M_{\mathrm{BB}}}$, respectively. Here, ω_{A} and ω_{B} are the transition angular frequencies of the two cavities. Finally, v_{Q} and i_{Q} represent the voltage of the superconducting island(s) and the persistent current of the qubit circuit. Depending on the specific qubit implementation, either v_{Q} or i_{Q} dominates, thus defining the charge and flux regimes.

B. Capacitance and inductance matrices up to second order

The matrices $\mathbf{C^{(n)}}$ and $\mathbf{M^{(n)}}$ account for corrections up to the nth-order interaction process between the elements of the network. In fact, in order to write the exact Hamiltonian of the circuit, all possible electromagnetic paths connecting its nodes must be considered. A consequence of this approach to circuit theory is that the direct coupling

$$\hat{H}_{\mathrm{AB}}^{(1)}=\hat{V}_{\mathrm{A}}c\hat{V}_{\mathrm{B}}+\hat{I}_{\mathrm{A}}m\hat{I}_{\mathrm{B}} \tag{2}$$

between resonators A and B [cf. Fig. 1(a)], here assumed to be weak, is not the only interaction mechanism to be considered. In fact, an indirect coupling mediated by the circuit associated with the qubit Q has to be also included in the Hamiltonian. The dominating term for the A-Q-B excitation pathway can be derived from its second-order electromagnetic energy [cf. Fig. 1(b)], which gives

$$\hat{H}_{\mathrm{AB}}^{(2)}=\hat{H}_{\mathrm{AB}}^{(1)}+\hat{V}_{\mathrm{A}}C_{\mathrm{AQ}}\frac{1}{C_{\mathrm{QQ}}}C_{\mathrm{QB}}\hat{V}_{\mathrm{B}}+\hat{I}_{\mathrm{A}}M_{\mathrm{AQ}}\frac{1}{M_{\mathrm{QQ}}}M_{\mathrm{QB}}\hat{I}_{\mathrm{B}}. \tag{3}$$

Note that the inverse path (B-Q-A) is already included in this equation. In our work, we assume $0\lesssim c\lesssim C_{\mathrm{AQ}}C_{\mathrm{QB}}/C_{\mathrm{QQ}}$ and $0\lesssim m\lesssim M_{\mathrm{AQ}}M_{\mathrm{QB}}/M_{\mathrm{QQ}}$ (cf. Sec. V). When $c,m\simeq0$, the direct coupling between A and B is negligible; i.e., the contribution of $\hat{H}_{\mathrm{AB}}^{(1)}$ can be omitted. On the other hand, when $c>0$ and/or $m>0$, both first- and second-order circuit theory contributions are relevant. In this case, c and m can represent a spurious or an engineered cross-talk. The latter can deliberately be exploited to increase the strength of the geometric second-order coupling. However, c and m should be small enough to leave the mode structure and quality factors of A and B unaffected.

From the knowledge of $\hat{H}_{\mathrm{AB}}^{(2)}$, the capacitance matrix up to second order is readily obtained,

$$\mathbf{C}^{(2)}=\begin{bmatrix} C_{\mathrm{AA}} & c+\dfrac{C_{\mathrm{AQ}}C_{\mathrm{QB}}}{C_{\mathrm{QQ}}} & C_{\mathrm{AQ}} \\ c+\dfrac{C_{\mathrm{BQ}}C_{\mathrm{QA}}}{C_{\mathrm{QQ}}} & C_{\mathrm{BB}} & C_{\mathrm{BQ}} \\ C_{\mathrm{QA}} & C_{\mathrm{QB}} & C_{\mathrm{QQ}} \end{bmatrix}. \tag{4}$$

The second-order corrections to the self-capacitances, i.e., the diagonal elements C_{kk}, are absorbed in their definitions[59] (cf. Sec. II C). In analogy, the corrected inductance matrix $\mathbf{M^{(2)}}$ is found by substituting C_{kl} with M_{kl} and c with m in matrix (4), yielding

$$\mathbf{M}^{(2)}=\begin{bmatrix} M_{\mathrm{AA}} & m+\dfrac{M_{\mathrm{AQ}}M_{\mathrm{QB}}}{M_{\mathrm{QQ}}} & M_{\mathrm{AQ}} \\ m+\dfrac{M_{\mathrm{BQ}}M_{\mathrm{QA}}}{M_{\mathrm{QQ}}} & M_{\mathrm{BB}} & M_{\mathrm{BQ}} \\ M_{\mathrm{QA}} & M_{\mathrm{QB}} & M_{\mathrm{QQ}} \end{bmatrix}. \tag{5}$$

Again, second-order corrections to the self-inductances are absorbed in the definition of M_{kk}. The matrices $\mathbf{C^{(2)}}$ and $\mathbf{M^{(2)}}$ constitute the *first main result* of this work. They show that if a strong qubit-resonator coupling (i.e., a vacuum Rabi coupling $\propto C_{\mathrm{AQ}},C_{\mathrm{QB}}$ for charge quantum circuits and $\propto M_{\mathrm{AQ}}$, M_{QB} for flux quantum circuits) is present, as in most circuit QED implementations,[1,3–12,24,25] a relevant geometric second-order coupling ($\propto C_{\mathrm{AQ}}C_{\mathrm{QB}}/C_{\mathrm{QQ}}$ or $\propto M_{\mathrm{AQ}}M_{\mathrm{QB}}/M_{\mathrm{QQ}}$ for charge and flux quantum circuits, respectively) has to be expected. This coupling becomes relevant in the dispersive regime,[22,24] where a dynamic second-order coupling, whose magnitude can be comparable to that of the geometric one, is also present (cf. Sec. III A). We study in detail the relationship between m and $M_{\mathrm{AQ}}M_{\mathrm{QB}}/M_{\mathrm{QQ}}$ in Sec. V. There, we show that for a realistic design engineered for a flux qubit, which is our experimental expertise,[12,58] the geometric second-order interaction dominates over the first-order one.

Figures 1(c)–1(e) show three generic sketches, where the coupling of two on-chip resonators to one superconducting qubit is illustrated. In particular, the sketch drawn in Fig. 1(c) is suitable when a flux qubit is intended to be utilized. In this case, the qubit is positioned at the current antinode of the first mode[60] of two $\lambda/2$ resonators. Moreover, this design clearly allows for engineering a strong coupling between the qubit and each resonator while reducing the geometric first-order coupling between resonators A and B. This is due to the fact that the two cavities are close to each other only in the restricted region where the qubit is located and then develop abruptly toward opposite directions. The sketch in Fig. 1(d), instead, is more suitable for charge qubit applications. The qubit can easily be fabricated near a voltage antinode.[1,22] Similar arguments as in the previous case apply for the qubit-resonator couplings and the geometric first-order coupling between A and B. Finally, the sketch in Fig. 1(e) relies on an

orthogonal-cavity design, which can be used for both charge and flux qubits. The main properties of such a setup were already presented in two of our previous works,[20,21] where orthogonal cavities were exploited for different purposes. In conclusion, we want to stress that based on the general sketches in Figs. 1(c)–1(e), a large variety of specific experimental implementations can be envisioned.

C. Role of circuit topology: Two examples

All results in Secs. II A and II B are general and do not rely *a priori* on the knowledge of the three-circuit network topology. Here, we explain with the aid of two easy examples how to obtain a reduced three-node network starting from a three-circuit one. The examples are based on the coupling of two superconducting coplanar waveguide or microstrip resonators to a single Cooper-pair box[1,22] (or a transmon[61–63]) or to a superconducting loop interrupted by one (or three) Josephson tunnel junction(s).[25,32,60,64]

The first example is the case of a single Cooper-pair box (a charge quantum circuit), which is formally equivalent to the more appealing case of the transmon. A single Cooper-pair box[1,22] is made of a superconducting island connected to a large reservoir via two Josephson tunnel junctions with Josephson energy E_J and capacitance C_J. The box is capacitively coupled to two resonators A and B by the gate capacitors C_{ga} and C_{gb}, respectively. In the charge basis, the Hamiltonian of a single Cooper-pair box can be written as[22]

$$\hat{H}_c = 4E_C \sum_n (\hat{n} - n_g)^2 |n\rangle\langle n| - \frac{E_J}{2} \sum_n (|n\rangle\langle n+1| + |n+1\rangle\langle n|), \tag{6}$$

where $E_C \equiv e^2/2C_\Sigma$ is the box electrostatic energy (e is the electron charge), $C_\Sigma \equiv C_{ga} + 2C_J + C_{gb}$ is its total capacitance,[65] $\langle n|\hat{n}|n\rangle$ represents the number of excess Cooper pairs on the island, and n_g is the global dimensionless gate charge applied to it. The latter is the sum of a dc signal n_g^{dc} (here, considered to be applied through cavity A) and a high-frequency excitation δn_g applied through cavities A and/or B, $n_g \equiv n_g^{\mathrm{dc}} + \delta n_g$. In particular, δn_g can represent the quantized electric fields (equivalent to the voltages) of the two cavities acting as quantum harmonic oscillators. Restricting ourselves to the two lowest charge states $n=0,1$, we can rewrite the Hamiltonian in Eq. (6) as

$$\begin{aligned}\hat{H}_c &= 2E_C(1 - 2n_g + 2n_g^2 + \hat{\tilde{\sigma}}_z - 2n_g\hat{\tilde{\sigma}}_z) - \frac{E_J}{2}\hat{\tilde{\sigma}}_x \\ &= 2E_C(1 - 2n_g^{\mathrm{dc}})\hat{\tilde{\sigma}}_z - \frac{E_J}{2}\hat{\tilde{\sigma}}_x \\ &\quad - 4E_C\delta n_g(1 - 2n_g^{\mathrm{dc}} - \delta n_g + \hat{\tilde{\sigma}}_z).\end{aligned} \tag{7}$$

The second line of the above equation forms the standard charge qubit, which can be controlled by the quasistatic bias $n_g^{\mathrm{dc}} \equiv C_{ga}v_{\mathrm{dc}}/2e$. The last expression contains four high-frequency interaction terms. Among those, two of them are particularly interesting.[66] These are $4E_C\delta n_g^2$ and $-4E_C\delta n_g\hat{\tilde{\sigma}}_z$. We now quantize the high-frequency excitations $\delta n_g \to \delta\hat{n}_g \equiv C_{ga}v_{\mathrm{A0}}(\hat{a}^\dagger + \hat{a})/2e + C_{gb}v_{\mathrm{B0}}(\hat{b}^\dagger + \hat{b})/2e$, using the fact that they are the quantized voltages of the two resonators. We subsequently perform a rotating-wave approximation (RWA) and, finally, write the interaction Hamiltonian

$$\begin{aligned}\hat{H}_c^{\mathrm{int}} &= \hbar G_{\mathrm{AB}}(\hat{a}^\dagger + \hat{a})(\hat{b}^\dagger + \hat{b}) - \hbar G_{\mathrm{A}}\hat{\tilde{\sigma}}_z(\hat{a}^\dagger + \hat{a}) \\ &\quad - \hbar G_{\mathrm{B}}\hat{\tilde{\sigma}}_z(\hat{b}^\dagger + \hat{b}) + \hbar\tilde{\omega}_{\mathrm{A}}\hat{a}^\dagger\hat{a} + \hbar\tilde{\omega}_{\mathrm{B}}\hat{b}^\dagger\hat{b},\end{aligned} \tag{8}$$

where all constant energy offsets, e.g., the Lamb shifts, have been neglected. Remarkably, in the first expression in the above equation we identify a geometric resonator-resonator interaction term with second-order coupling coefficient $G_{\mathrm{AB}} \equiv v_{\mathrm{A0}}v_{\mathrm{B0}}C_{ga}C_{gb}/C_\Sigma\hbar$. Furthermore, the second and third expressions in this equation represent the expected first-order qubit-resonator interactions with coupling coefficients $G_{\mathrm{A}} \equiv e(C_{ga}/C_\Sigma)v_{\mathrm{A0}}/\hbar$ and $G_{\mathrm{B}} \equiv e(C_{gb}/C_\Sigma)v_{\mathrm{B0}}/\hbar$. In the last two expressions, the two small renormalizations $\tilde{\omega}_{\mathrm{A}} \equiv (C_{ga}v_{\mathrm{A0}})^2/C_\Sigma\hbar$ and $\tilde{\omega}_{\mathrm{B}} \equiv (C_{gb}v_{\mathrm{B0}})^2/C_\Sigma\hbar$ of the resonator angular frequencies are artifacts due to the simple model behind the Hamiltonian in Eq. (6). A more advanced model based on a realistic circuit topology yields similar renormalization terms, which, however, are governed by different topology-dependent constants. Among the possible ways to find the correct constants, we choose the circuit transformations in Figs. 2(a)–2(c). This approach also allows us to better understand the geometric second-order interaction term.

In Fig. 2(a), the two cavities are represented as LC resonators with total capacitances and inductances C_{ra} and C_{rb} and L_{ra} and L_{rb}, respectively. The quantized voltages and currents of the two resonators are $\hat{V}_{ra} \equiv v_{\mathrm{A0}}(\hat{a}^\dagger + \hat{a})$, $\hat{V}_{rb} \equiv v_{\mathrm{B0}}(\hat{b}^\dagger + \hat{b})$, $\hat{I}_{ra} \equiv i_{\mathrm{A0}}j(\hat{a}^\dagger - \hat{a})$, and $\hat{I}_{rb} \equiv i_{\mathrm{B0}}j(\hat{b}^\dagger - \hat{b})$, respectively. Also, C_{ab} accounts for a first-order cross capacitance between resonators A and B, which, for simplicity, is neglected in Eqs. (7) and (8). In addition, here we are interested only in the geometric properties of the charge quantum circuit. The dynamic properties of this circuit are studied following a more canonical approach within a two-level approximation in Sec. III. The dynamic properties are governed by the two Josephson tunnel junctions and by the number of excess Cooper pairs on the island, $\langle n|\hat{n}|n\rangle$. To simplify our derivations, we can then assume $\hat{n}=0$ and consider only the capacitance C_J of the two Josephson tunnel junctions but not their Josephson energy.

We now derive in three steps the geometric part of the interaction Hamiltonian by means of circuit theory. The procedure is visualized in Figs. 2(a)–2(c). The steps are as follows:

(i) First, we assume that the circuit associated to the charge qubit is positioned at a voltage antinode[22] of both resonators. Consequently, we can replace the two current sources in Fig. 2(a) with open circuits, $\hat{I}_{ra} = \hat{I}_{rb} = 0$. Thus, we can eliminate both L_{ra} and L_{rb} from the circuit diagram because they are in series with open circuits.

(ii) Second, we apply the superposition principle of circuit theory.[57] One at the time, we replace each of the two voltage sources with short circuits, $\hat{V}_{ra}=0$ or $\hat{V}_{rb}=0$. This allows us to split up the circuit in Fig. 2(a) into the two subcircuits in Fig. 2(b), which are topologically less complex. As a conse-

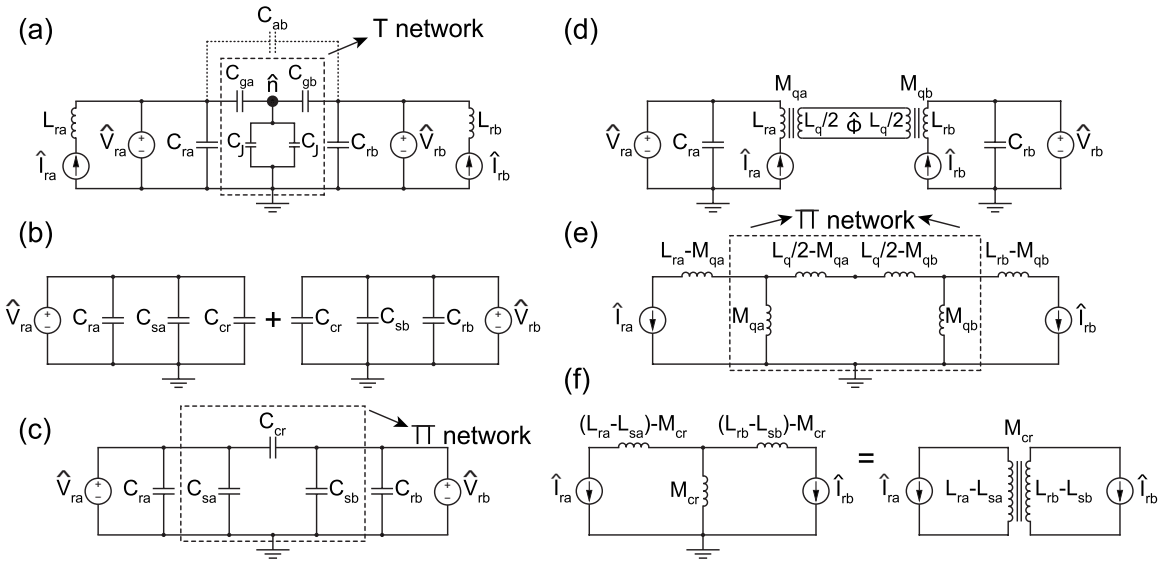

FIG. 2. Equivalent circuit diagrams for two different implementations of two-resonator circuit QED based on either a charge qubit [(a)–(c)] or a flux qubit [(d)–(f)]. Cf. Sec. II C for details. (a) $\hat{V}_{ra}$ and $\hat{V}_{rb}$: Quantized voltage sources associated with resonators A and B parallel to the self-capacitances C_{ra} and C_{rb} of the resonators. $\hat{I}_{ra}$ and $\hat{I}_{rb}$: Quantized current sources associated with resonators A and B in series with the self-inductances L_{ra} and L_{rb} of the resonators. The number of excess Cooper pairs on the charge qubit island (big dot) is $\langle n|\hat{n}|n\rangle$. C_J: Capacitance of each of the two Josephson tunnel junctions connecting the island to ground. C_{ga} and C_{gb}: Coupling capacitances between the qubit and the two resonators. C_{ab}: First-order cross capacitance between A and B (typically small; dotted line). The dashed box marks a T network composed of C_{ga}, $2C_J$, and C_{gb}. (b) $C_{\rm cr}\equiv C_{ga}C_{gb}/C_\Sigma$: Second-order cross capacitance. $C_{sa}\equiv 2C_JC_{ga}/C_\Sigma$ and $C_{sb}\equiv 2C_JC_{gb}/C_\Sigma$: Resonator shift capacitances. C_{ab} is neglected for simplicity. (c) The circuits in (b) rearranged as a single Π network (dashed box). The latter is equivalent to the T network in (a). The magnitudes of C_{ra} and C_{rb} are increased by the presence of the shift capacitances C_{sa} and C_{sb}. (d) Two resonators A and B inductively coupled via M_{qa} and M_{qb} to a flux qubit with total self-inductance $L_q=L_q/2+L_q/2$ and flux operator $\hat{\Phi}$. The first-order mutual inductance m between the two resonators is neglected to simplify the notation. (e) The disconnected circuit in (d) is transformed into a connected circuit (Ref. 57). Again, we can identify a Π network (dashed box). (f) Left side: T network obtained from the Π network in (e). We identify the second-order mutual inductance $M_{\rm cr}\equiv M_{qa}M_{qb}/L_q$ and the shift inductances $L_{sa}\equiv M_{qa}^2/L_q$ and $L_{sb}\equiv M_{qb}^2/L_q$. Right side: The connected circuit on the left side is transformed into a disconnected circuit (Ref. 57).

quence, in the respective subcircuits, C_{rb} or C_{ra} can be substituted with short circuits and all other capacitors opportunely rearranged. In this way, for the case of cavity A, we find the small shift capacitance $C_{sa}\equiv 2C_JC_{ga}/C_\Sigma$, which gives the correct angular frequency renormalization of the resonator, $\tilde{\omega}_{\rm A}^{\rm corr}\equiv 2C_JC_{ga}v_{\rm A0}^2/C_\Sigma\hbar$. Remarkably, we also find the second-order cross capacitance $C_{\rm cr}\equiv C_{ga}C_{gb}/C_\Sigma$, corresponding to the geometric second-order coupling between the resonators. This is equivalent to the result obtained in Eq. (3) in Sec. II B and is consistent with the simple model of Eqs. (6)–(8). We notice that $C_{\rm cr}$ deviates from the simple series of the two gate capacitances C_{ga} and C_{gb} because of the presence of C_J in C_Σ. For the case of cavity B, $C_{sb}\equiv 2C_JC_{gb}/C_\Sigma$ and $\tilde{\omega}_{\rm B}^{\rm corr}\equiv 2C_JC_{gb}v_{\rm B0}^2/C_\Sigma\hbar$ can be derived in an analogous manner. In Sec. II B, the two renormalization constants as well as C_J are absorbed in the definitions of $C_{\rm AA}$, $C_{\rm BB}$, and $C_{\rm QQ}$, respectively.

(iii) Third, we notice that the cross capacitance $C_{\rm cr}$, which is responsible for the geometric second-order interaction between A and B, is subjected to both quantum voltages $\hat{V}_{ra}$ and $\hat{V}_{rb}$. Hence, we can finally draw the circuit diagram in Fig. 2(c). Indeed, we could have identified the T network in Fig. 2(a) (indicated by a dashed box) and transformed it into the equivalent Π network in Fig. 2(c) (also indicated by a dashed box) in a single step,[57] obtaining the same results. We prefer to explicitly show the steps in Fig. 2(b) for pedagogical reasons.

The *second example* is based on a superconducting loop interrupted by one Josephson tunnel junction (a flux quantum circuit). Such a device is also known as radio-frequency (rf) superconducting quantum interference device (SQUID). We choose the rf SQUID here for pure pedagogical reasons. In fact, our treatment could be extended to the more common case of three junctions.[67,68] The Hamiltonian of an rf SQUID can be expressed as[26,27,32,60]

$$\hat{H}_f=\frac{\hat{Q}^2}{2C_J}+\frac{(\hat{\Phi}-\Phi_x)^2}{2L_q}-E_J\cos\left(2\pi\frac{\hat{\Phi}}{\Phi_0}\right),\qquad(9)$$

where $\hat{Q}$ is the operator for the charge accumulated on the capacitor C_J associated with the Josephson tunnel junction. The flux operator $\hat{\Phi}$ is the conjugated variable of $\hat{Q}$, i.e., $[\hat{\Phi},\hat{Q}]=j\hbar$. In analogy to the dimensionless gate charge n_g of the previous example, the flux bias $\Phi_x\equiv\Phi_x^{\rm dc}+\delta\Phi_x$ consists of a dc and an ac component. The self-inductance of the superconducting loop is defined as L_q. When the rf SQUID is coupled to two quantized resonators, we can quantize the high-frequency excitations performing the transformations $\delta\Phi_x\to\delta\hat{\Phi}_x\equiv M_{qa}i_{\rm A0}j(\hat{a}^\dagger-\hat{a})+M_{qb}i_{\rm B0}j(\hat{b}^\dagger-\hat{b})$. Here, M_{qa} and

TABLE I. Relevant parameters for a possible two-resonator circuit QED setup based on a superconducting flux qubit. The various constants are described in Sec. V and reported in Fig. 2. All inductances are simulated using the version of FASTHENRY for superconducting materials (Ref. 92). The capacitances are calculated analytically. All second-order inductances are computed analytically and numerically and then compared to each other for consistency. We find excellent agreement between the estimates $M_{qa}M_{qb}/L_q$ and $\tilde{m}-m$ for the second-order mutual inductance. Also, the shift inductances M_{qa}^2/L_q and M_{qb}^2/L_q coincide with their counterparts $L_{sa}\equiv L_{rb}^*-\tilde{L}_{ra}^*$ and $L_{sb}\equiv L_{rb}^*-\tilde{L}_{rb}^*$, respectively. These parameters are suitable for the implementation of a superconducting quantum switch.

L_{ra}^* (pH)	L_{ra} (nH)	C_{ra} (pF)	λ_A (mm)	$i_{A0}\equiv\sqrt{\hbar\omega_A/2L_{ra}}$ (nA)	L_q (pH)	M_{qa} (pH)	$M_{qa}M_{qb}/L_q$ (pH)	$+L_{sa}\equiv M_{qa}^2/L_q$ (pH)	$+L_{sb}\equiv M_{qb}^2/L_q$ (pH)
252.781	6.066 74	3.363 69	24	13.8251	784.228	61.2387	4.781 92	+4.782 00	+4.781 84
L_{rb}^* (pH)	L_{rb} (nH)	C_{rb} (pF)	λ_B (mm)	$i_{B0}\equiv\sqrt{\hbar\omega_B/2L_{rb}}$ (nA)	m (pH)	M_{qb} (pH)	$\tilde{m}-m$ (pH)	$-L_{sa}=\tilde{L}_{ra}^*-L_{ra}^*$ (pH)	$-L_{sb}=\tilde{L}_{rb}^*-L_{rb}^*$ (pH)
252.778	6.066 67	3.363 69	24	13.8252	2.901 30	61.2377	4.781 92	−4.781 00	−4.781 00

M_{qb} are the mutual inductances between the loop and each resonator. We can then assume $\hat{\Phi}=0$, perform a two-level approximation and a RWA, and finally obtain the same interaction Hamiltonian as in Eq. (8). However, in this case the coefficients are redefined as $\tilde{\omega}_A\equiv(M_{qa}i_{A0})^2/L_q\hbar$, $\tilde{\omega}_B\equiv(M_{qb}i_{B0})^2/L_q\hbar$, and $G_{AB}\equiv i_{A0}i_{B0}M_{qa}M_{qb}/L_q\hbar$. The term with coupling coefficient G_{AB} constitutes the geometric second-order interaction between A and B. As it appears clear from the discussion below, once again the renormalization terms $\tilde{\omega}_A$ and $\tilde{\omega}_B$ do not catch the circuit topology properly. This issue can be clarified by analyzing the circuit diagram drawn in Fig. 2(d), where all the geometric elements for this example are shown. The first-order mutual inductance m between the two resonators is neglected to simplify the notation. Again, the Josephson tunnel junctions responsible for the dynamic behavior are not included.

We now study the geometric part of the interaction Hamiltonian between the rf SQUID and the two resonators, following a similar path as for the case of the single Cooper-pair box [cf. Figs. 2(d)–2(f)]. The four main transformation steps are as follows:

(i) First, we assume the circuit corresponding to the flux qubit to be positioned at a current antinode. Thus, in Fig. 2(e), we replace all voltage sources and capacitors in Fig. 2(d) with short circuits. The self-inductance of the qubit loop is split up into two $L_q/2$ inductances to facilitate the following transformation steps.

(ii) Second, a well-known theorem of circuit theory[57] allows us to transform the three disconnected circuits in Fig. 2(d) into the connected circuit in Fig. 2(e). Here, the region indicated by the dashed box evidently forms a Π network.

(iii) Third, a Π-to-T-network transformation[57] results in the circuit on the left side of Fig. 2(f).

(iv) Fourth, applying the inverse theorem of that used in step (ii) finally allows us to draw the equivalent circuit on the right side of Fig. 2(f). Here, $M_{cr}\equiv M_{qa}M_{qb}/L_q$ represents the second-order mutual inductance between resonators A and B, corresponding to the geometric second-order coupling between them. Remarkably, this coincides with our result obtained in Eq. (3) in Sec. II B and is consistent with the simple model of Eq. (9). However, in this model the small shift inductances $L_{sa}\equiv M_{qa}^2/L_q$ and $L_{sb}\equiv M_{qb}^2/L_q$ (here defined to be strictly positive) acquire the wrong sign. Our circuit approach reveals that the correct renormalization constants of the resonators' angular frequency are $\tilde{\omega}_A=-L_{sa}i_{A0}^2/\hbar$ and $\tilde{\omega}_B=-L_{sb}i_{B0}^2/\hbar$. This result is also confirmed by our numerical simulations (cf. Sec. V and Table I). In Sec. II B, these renormalization constants are absorbed in the definitions of M_{AA} and M_{BB}.

III. DERIVATION OF THE QUANTUM SWITCH HAMILTONIAN

In this section, we analyze the Hamiltonian of a three-node quantum network as found in Sec. II B. In particular, we focus on the relevant case of large qubit-resonator detuning, i.e., the dispersive regime of two-resonator circuit QED. Under this assumption, we are able to derive an effective Hamiltonian describing a quantum switch between two resonators. We compare the analytical results to those of extensive simulations (cf. Sec. III A). We also propose a protocol for the quantum switch operation stressing two possible variants. One is based on a qubit population inversion and the other on an adiabatic-shift pulse with the qubit in the energy ground state (cf. Sec. III B). Finally, we give a few examples of advanced applications of the quantum switch and, in general, of dispersive two-resonator circuit QED (cf. Sec. III C).

A. Balancing the geometric and dynamic couplings

We now give the total Hamiltonian of the three-node quantum network in Figs. 1(a) and 1(b). In order to avoid unnecessarily cumbersome calculations, we restrict ourselves to purely inductive interactions up to geometric second-order corrections. In this framework, the most suitable quantum circuit to be used is a flux qubit. Hereafter, all specific parameters and corresponding simulations refer to this particular case. Nevertheless, the formalism which we develop remains general and can be extended to purely capacitive interactions (charge qubits) straightforwardly.

The flux qubit is assumed to be positioned at a current antinode. As a consequence, the vacuum fluctuations i_{A0} and i_{B0} have maximum values i_{A0}^{max} and i_{B0}^{max} at the qubit position and we can impose $v_{A0}=v_{B0}=0$. Also, in the standard operation of a flux qubit no dc voltages are applied, i.e., $v_{dc}=0$, and the quasistatic flux bias is usually controlled by an ex-

ternal coil and not by the cavities (cf. Sec. II A). Again, we impose $i_{dc}=0$ and add to the Hamiltonian in Eq. (1) the term $(\Phi_x^{dc}-\Phi_0/2)\hat{I}_Q$. Under all these assumptions and substituting $\mathbf{M}^{(n)}$ of Eq. (1) with $\mathbf{M}^{(2)}$ of matrix (5), we readily obtain

$$\hat{H}' = \frac{1}{2}\hbar\epsilon\hat{\bar{\sigma}}_z + \frac{1}{2}\hbar\delta_Q\hat{\bar{\sigma}}_x + \hbar\omega_A\hat{a}^\dagger\hat{a} + \hbar\omega_B\hat{b}^\dagger\hat{b} + \hbar g_A\hat{\bar{\sigma}}_z(\hat{a}^\dagger+\hat{a}) + \hbar g_B\hat{\bar{\sigma}}_z(\hat{b}^\dagger+\hat{b}) + \hbar g_{AB}(\hat{a}^\dagger+\hat{a})(\hat{b}^\dagger+\hat{b}). \quad (10)$$

Here, all global energy offsets have been neglected and we have included both first- and second-order circuit theory contributions. In this equation, $\hbar\epsilon \equiv 2i_Q(\Phi_x^{dc}-\Phi_0/2)$ is the qubit energy bias, $\delta_Q \equiv \delta_Q(E_c,E_J)$ is the qubit gap,[26,67] $\omega_A \equiv 1/\sqrt{M_{AA}C_{AA}}$ and $\omega_B \equiv 1/\sqrt{M_{BB}C_{BB}}$ are the angular frequencies of resonators A and B, respectively, $g_A \equiv i_Q i_{A0} M_{AQ}/\hbar$ and $g_B \equiv i_Q i_{B0} M_{BQ}/\hbar$ are the qubit-resonator coupling coefficients, and, finally, the second-order coupling coefficient $g_{AB} \equiv i_{A0} i_{B0}(m+M_{AQ}M_{QB}/M_{QQ})/\hbar$. In general, g_A and g_B can be different due to parameter spread during the sample fabrication. Later, we show that the architecture proposed here is robust with respect to such imperfections. We now rotate the system Hamiltonian in Eq. (10) into the qubit energy eigenbasis $\{|g\rangle,|e\rangle\}$ obtaining

$$\hat{H} = \hbar\frac{\Omega_Q}{2}\hat{\sigma}_z + \hbar\omega_A\hat{a}^\dagger\hat{a} + \hbar\omega_B\hat{b}^\dagger\hat{b} + \hbar g_A\cos\theta\,\hat{\sigma}_z(\hat{a}^\dagger+\hat{a}) + \hbar g_B\cos\theta\,\hat{\sigma}_z(\hat{b}^\dagger+\hat{b}) - \hbar g_A\sin\theta\,\hat{\sigma}_x(\hat{a}^\dagger+\hat{a}) - \hbar g_B\cos\theta\,\hat{\sigma}_x(\hat{b}^\dagger+\hat{b}) + \hbar g_{AB}(\hat{a}^\dagger+\hat{a})(\hat{b}^\dagger+\hat{b}). \quad (11)$$

Here, $\Omega_Q \equiv \sqrt{\epsilon^2+\delta_Q^2}$ is the Φ_x^{dc}-dependent transition frequency of the qubit and $\theta \equiv \arctan(\delta_Q/\epsilon)$ is the usual mixing angle. Hereafter, we use the redefined Pauli operators $\hat{\sigma}_x$ and $\hat{\sigma}_z$, where $\hat{\sigma}_x=\hat{\sigma}^+ + \hat{\sigma}^-$, $\hat{\sigma}_z=\hat{\sigma}^+\hat{\sigma}^- - \hat{\sigma}^-\hat{\sigma}^+$, and $\hat{\sigma}^+$ and $\hat{\sigma}^-$ are the lowering and raising operators between the qubit energy ground state $|g\rangle$ and excited state $|e\rangle$, respectively. Expressing $\hat{H}$ in an interaction picture with respect to the qubit and both resonators, $\hat{a}^\dagger \to \hat{a}^\dagger \exp(+j\omega_A t)$, $\hat{a} \to \hat{a}\exp(-j\omega_A t)$, $\hat{b}^\dagger \to \hat{b}^\dagger \exp(+j\omega_B t)$, $\hat{b} \to \hat{b}\exp(-j\omega_B t)$, and $\hat{\sigma}^\mp \to \hat{\sigma}^\mp \exp(\mp j\Omega_Q t)$, assuming $\omega_A=\omega_B \equiv \omega \equiv 2\pi f$, and performing a RWA yields

$$\hat{\tilde{H}} = \hbar\sin\theta\,[\hat{\sigma}^-(g_A\hat{a}^\dagger + g_B\hat{b}^\dagger)e^{-j\Delta t} + \hat{\sigma}^+(g_A\hat{a}+g_B\hat{b})e^{j\Delta t}] + \hbar g_{AB}(\hat{a}^\dagger\hat{b}+\hat{a}\hat{b}^\dagger). \quad (12)$$

Here, $\Delta \equiv \Omega_Q - \omega$ is the qubit-resonator detuning. The first two terms of Eq. (12) represent a standard two-mode JC dynamics.[30,69] The last term, instead, constitutes a beam-splitter-type interaction specific to two-resonator circuit QED. This interaction is not present in the quantum-optical version.[30,69] The coupling coefficient g_{AB} is typically much smaller than g_A and g_B (see below). However, in the dispersive regime ($|\Delta| \gg \max\{g_A,g_B,g_{AB}\}$), g_{AB} becomes comparable to all other dispersive coupling strengths. To gain further insights into this matter, we can define two superoperators $\hat{\tilde{\Xi}}^\dagger \equiv \hat{\sigma}^+(g_A\hat{a}+g_B\hat{b})$ and $\hat{\tilde{\Xi}} \equiv \hat{\sigma}^-(g_A\hat{a}^\dagger+g_B\hat{b}^\dagger)$. It can be shown that the Dyson series for the evolution operator associated with the time-dependent Hamiltonian in Eq. (12) can be rewritten in the exponential form $\hat{U}=\exp(-j\hat{\tilde{H}}_{eff}t/\hbar)$, where $\hat{\tilde{H}}_{eff}=\hbar[\hat{\tilde{\Xi}}^\dagger,\hat{\tilde{\Xi}}]/\Delta + \hbar g_{AB}(\hat{a}^\dagger\hat{b}+\hat{a}\hat{b}^\dagger)$. Thus

$$\hat{\tilde{H}}_{eff} = \hbar\frac{(g_A\sin\theta)^2}{\Delta}\hat{\sigma}_z\left(\hat{a}^\dagger\hat{a}+\frac{1}{2}\right) + \hbar\frac{(g_B\sin\theta)^2}{\Delta}\hat{\sigma}_z\left(\hat{b}^\dagger\hat{b}+\frac{1}{2}\right) + \hbar\left(\frac{g_A g_B\sin^2\theta}{\Delta}\hat{\sigma}_z + g_{AB}\right)(\hat{a}^\dagger\hat{b}+\hat{a}\hat{b}^\dagger). \quad (13)$$

In this Hamiltonian, the first two terms represent dynamic (ac-Zeeman) shifts (ac-Stark shifts in the case of charge qubits) of the transition angular frequency of resonators A and B, respectively. If $g_A=g_B \equiv g$ and we only use eigenstates of $\hat{\sigma}_z$, the first and second terms of Eq. (13) equally renormalize ω_A and ω_B, respectively. The Hamiltonian in Eq. (13) can be further simplified through an additional unitary transformation described by $\hat{U}_0=\exp(j\hat{H}_0 t/\hbar)$, where $\hat{H}_0 \equiv \hbar(g_A^2\sin^2\theta/\Delta)\hat{\sigma}_z(\hat{a}^\dagger\hat{a}+1/2)+\hbar(g_B^2\sin^2\theta/\Delta)\hat{\sigma}_z(\hat{b}^\dagger\hat{b}+1/2)$. When $g_A=g_B \equiv g$, this transformation yields the final effective Hamiltonian

$$\hat{H}_{eff} = \hbar\left(\frac{g^2\sin^2\theta}{\Delta}\hat{\sigma}_z + g_{AB}\right)(\hat{a}^\dagger\hat{b}+\hat{a}\hat{b}^\dagger), \quad (14)$$

which constitutes the *second main result* of this work. This Hamiltonian is the key ingredient for the implementation of a quantum switch between the two resonators. In fact, it clearly represents a tunable interaction between A and B characterized by the effective coupling coefficients

$$g_{sw}^{|g\rangle} \equiv g_{AB} - \frac{g^2\sin^2\theta}{\Delta}, \qquad g_{sw}^{|e\rangle} \equiv g_{AB} + \frac{g^2\sin^2\theta}{\Delta} \quad (15)$$

for the qubit in $|g\rangle$ or $|e\rangle$, respectively. The switching of such an interaction triggers, or prevents, the exchange of quantum information between A and B. On the one hand, the first part of this interaction is a purely geometric coupling, which is constant and qubit-state independent. On the other hand, the second part is a dynamic coupling, which depends on the state of the qubit. The *switch setting condition*

$$\frac{g^2\sin^2\theta}{|\Delta|} = |g_{AB}| \quad (16)$$

can easily be fulfilled varying Δ, changing $\sin\theta$, or inducing ac-Zeeman or -Stark shifts.[6] In the special case of a charge qubit, not treated here in detail, this task can also be accomplished by modifying the qubit transition angular frequency Ω_Q via a suitable quasistatic magnetic field.[1] This allows one to keep the qubit at the degeneracy point. Here, we focus on the first option, i.e., finding a suitable qubit bias for which the detuning Δ fulfills the relation in Eq. (16). For a flux qubit, this can be realized by polarizing the qubit by means of an external flux.

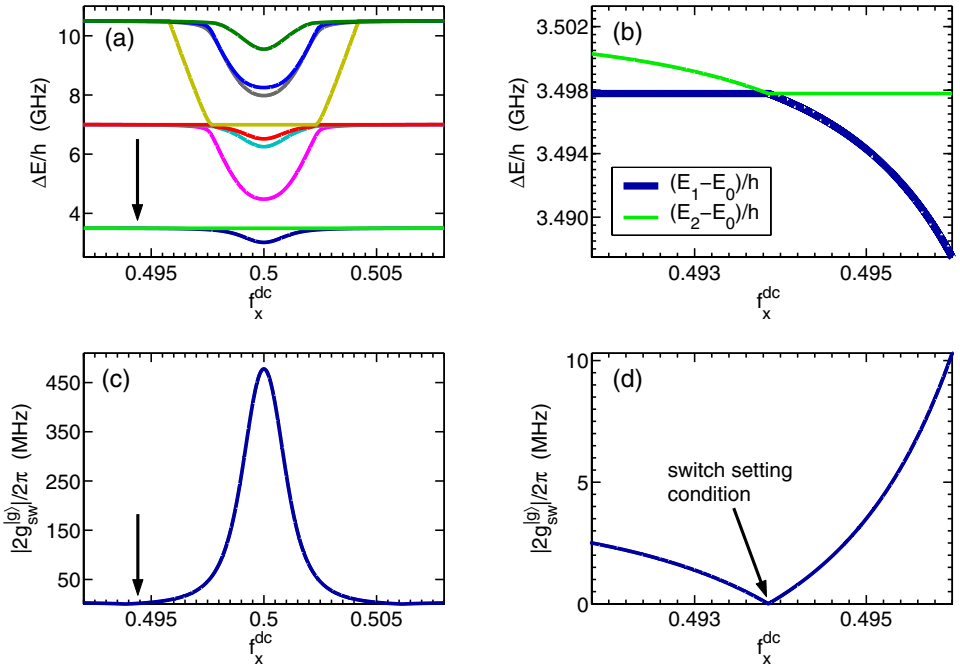

FIG. 3. (Color online) Simulation of the Hamiltonian in Eq. (10) in the dispersive regime (cf. Sec. III A for a detailed description of the system parameters). (a) The differences between the first nine excited energy levels of the quantum switch Hamiltonian and the ground-state energy level, ΔE, as a function of the frustration $f_x^{\mathrm{dc}} \equiv \Phi_x^{\mathrm{dc}}/\Phi_0$. The two lowest lines [blue (dark gray) and green (light gray), respectively] are associated with resonators A and B. The dispersive action of the qubit, which modifies the shape of the resonator lines, is clearly noticeable in the vicinity of the qubit degeneracy point. In this region, the third energy difference [hyperbolic shape, magenta (middle gray) line] represents the modified transition frequency of the qubit. (b) Closeup of the area indicated by the black arrow in (a). Here, the two modified resonator lines [thick blue (dark gray) and thin green (light gray)] cross each other. (c) Quantum switch coupling coefficient $|2g_{\mathrm{sw}}^{|g\rangle}|$ extrapolated from the energy spectrum in (a) plotted versus f_x^{dc}. (d) Closeup of the area indicated by the black arrow in (c). The switch setting condition $|2g_{\mathrm{sw}}^{|g\rangle}|=0$ is reached at $f_x^{\mathrm{dc}} \simeq 0.4938$.

To better understand the switch setting condition, we numerically diagonalize the entire system Hamiltonian in Eq. (10), without performing any approximation. The results are presented in Fig. 3, which shows the energy spectrum of the quantum switch Hamiltonian and the effective coupling coefficient $|2g_{\mathrm{sw}}^{|g\rangle}|$ for a flux qubit with $i_{\mathrm{Q}}=370$ nA, $\delta_{\mathrm{Q}}/2\pi=4$ GHz, $f=3.5$ GHz, $g/2\pi=472$ MHz, and $g_{\mathrm{AB}}/2\pi=2.2$ MHz. The parameters for the flux qubit are chosen from our previous experimental works,[12,58] whereas the three coupling coefficients are the result of detailed simulations (cf. Sec. V). It is worth mentioning that large vacuum Rabi couplings $g/2\pi$ on the order of 500 MHz have already been achieved both for flux and charge qubits.[4,25] We have chosen the qubit to be already detuned from both resonators by 0.5 GHz when biased at the flux degeneracy point. Moving sufficiently far from the qubit degeneracy point enables us to increase the qubit-resonator detuning such that the system can be modeled by the Hamiltonian in Eq. (14).

Figure 3(a) shows the differences between the first nine excited energy levels of the quantum switch Hamiltonian and the ground-state energy level, $\Delta E_i \equiv E_i - E_0$, with $i=\{1,\ldots,10\}$, as a function of the frustration $f_x \equiv \Phi_x^{\mathrm{dc}}/\Phi_0$. Here, E_i is the energy level of the ith excited state and E_0 is that of the ground state. Due to the qubit-resonator detuning, the two lowest energy differences [blue (dark gray) and green (light gray) lines] correspond to the modified transition frequencies of the two resonators. Owing to the interaction with the qubit, these lines are not flat. This effect becomes particularly evident in the region close to the qubit degeneracy point, where dispersivity is reduced. In this region, the third energy difference [hyperbolic shape, magenta (middle gray) line) represents the modified transition frequency of the qubit. When moving away from the qubit degeneracy point, a crossing between the modified resonator lines is encountered, as clearly shown in Fig. 3(b) [see thick blue (dark gray) and thin green (light gray) lines]. This crossing represents the switch setting condition in Eq. (16). Figures 3(c) and 3(d) show the absolute value of the flux-dependent coupling coefficient $|2g_{\mathrm{sw}}^{|g\rangle}|$ in the frustration windows in Figs. 3(a) and 3(b), respectively. The switch setting condition $|2g_{\mathrm{sw}}^{|g\rangle}|=0$ is reached at $f_x^{\mathrm{dc}} \simeq 0.4938$.

A comparison between the analytic expression in Eq. (15) with the qubit in $|g\rangle$ [dashed green (light gray) lines] and a numerical estimate of the effective coupling coefficient $|2g_{\mathrm{sw}}^{|g\rangle}|$ [solid blue (dark gray) lines] is shown in Fig. 4. To clarify similarities and differences between analytical and numerical calculations, we choose two different sets of parameters. In Fig. 4(a), the center frequencies of the two resonators are set to be $f_{\mathrm{A}}=f_{\mathrm{B}}=f=2.7$ GHz, which implies a reduced $g/2\pi \simeq 364$ MHz and $g_{\mathrm{AB}} \simeq 1.3$ MHz. All the other parameters are equal to those used to obtain the results in Fig. 3. In Fig. 4(b), we use the same set of parameters utilized to obtain the results in Fig. 3, i.e., $f_{\mathrm{A}}=f_{\mathrm{B}}=f=3.5$ GHz and the corresponding coupling doefficients. In

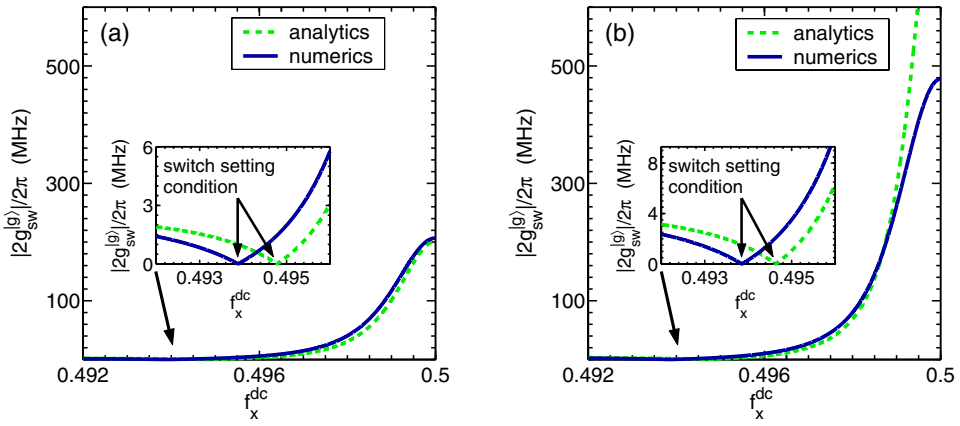

FIG. 4. (Color online) Comparison between the f_x^{dc} dependence of the analytical expression for the effective coupling coefficient $|2g_{\mathrm{sw}}^{|g\rangle}|$ obtained from Eq. (15) and the one found by numerically diagonalizing the Hamiltonian in Eq. (10). (a) We choose a center frequency $f_A=f_B=f=2.7$ GHz for the two resonators, which implies a reduced $g/2\pi\simeq 364$ MHz and $g_{AB}\simeq 1.3$ MHz. All the other parameters are equal to those used to obtain the results in Fig. 3. The analytical [dashed green (light gray) line] and the numerical [solid blue (dark gray) line] results are in excellent agreement. In the large-detuning limit far away from the qubit degeneracy point, $|2g_{\mathrm{sw}}^{|g\rangle}|$ saturates to the value $|2g_{AB}|\simeq 2.6$ MHz. Inset: Closeup of the region near the switch setting condition. (b) Here, we use the same set of parameters utlized to obtain the results in Fig. 3, i.e., a center frequency $f_A=f_B=f=3.5$ GHz for the two resonators and the corresponding coupling coefficients. The analytical [dashed green (light gray) line] and numerical [solid blue (dark gray) line] results are in good agreement away from the qubit degeneracy point. Closer to it they diverge (cf. Sec. III A for more details). In the large-detuning limit far away from the qubit degeneracy point, $|2g_{\mathrm{sw}}^{|g\rangle}|$ saturates to the value $|2g_{AB}|\simeq 4.4$ MHz. Inset: Closeup of the region near the switch setting condition.

Fig. 4(a), analytics and numerics agree over the entire frustration window. The inset shows that the switch setting condition obtained from the numerical simulation is only slightly shifted with respect to the analytical prediction. Also in Fig. 4(b), the agreement between analytical and numerical estimates is good far away from the qubit degeneracy point. However, closer to it the qubit and the two resonators are not detuned enough to guarantee dispersivity. Therefore, analytics and numerics start to deviate, as expected. Again, the inset shows that the switch setting condition can be fulfilled. It is worth pointing out that both analytical and numerical estimates converge to the value $|2g_{AB}|$ in the limit of large detuning. We find $|2g_{AB}|/2\pi\simeq 2.6$ MHz and $|2g_{AB}|/2\pi\simeq 4.4$ MHz from the simulations that produce Figs. 4(a) and 4(b), respectively. Additionally, we have two important remarks on the results shown in Figs. 4(a) and 4(b). First, the change of the coupling constants g and g_{AB} between the two parameter sets is a direct consequence of altering the resonator frequency. Although the mutual inductances remain unaffected, the vacuum (zero-point) currents are changed. Second, the fact that the switch setting condition occurs at almost the same frustration value for both parameters sets is due to our specific choice of these parameters.

Finally, we demonstrate that the quantum switch Hamiltonian is robust against parameter spread due to fabrication inaccuracies. Typically, for a center frequency of 5 GHz, the expected spread around this value is approximately[70] ∓ 10 MHz for two resonators fabricated on the same chip. Also, the coupling coefficients g_A and g_B can differ slightly. In this case, a generalized effective Hamiltonian for the quantum switch can be derived,[23]

$$\hat{H}_{\mathrm{eff}}^{\mathrm{gen}}=\hbar\frac{(g_A\sin\theta)^2}{\Delta_A}\hat{\sigma}_z\hat{a}^\dagger\hat{a}+\hbar\frac{(g_B\sin\theta)^2}{\Delta_B}\hat{\sigma}_z\hat{b}^\dagger\hat{b}+\hbar\left[\frac{g_Ag_B\sin^2\theta}{2}\left(\frac{1}{\Delta_A}+\frac{1}{\Delta_B}\right)\hat{\sigma}_z+g_{AB}\right]\times(\hat{a}^\dagger\hat{b}e^{+j\delta_{AB}t}+\hat{a}\hat{b}^\dagger e^{-j\delta_{AB}t}),\tag{17}$$

where $\Delta_A\equiv\Omega_Q-\omega_A$, $\Delta_B\equiv\Omega_Q-\omega_B$, and $\delta_{AB}\equiv\omega_A-\omega_B$. From Eq. (17), we can deduce the generalized coupling coefficient of the switch, $g_{\mathrm{sw}}^{|g\rangle,|e\rangle}\equiv g_{AB}\mp g_Ag_B\sin^2\theta(1/2\Delta_A+1/2\Delta_B)$ for the qubit in the ground state $|g\rangle$ or excited state $|e\rangle$, respectively. As a consequence, the *generalized switch setting condition* becomes

$$\left|\frac{g_Ag_B\sin^2\theta}{2}\left(\frac{1}{\Delta_A}+\frac{1}{\Delta_B}\right)\right|=|g_{AB}|.\tag{18}$$

This condition is displayed in Fig. 5 [dashed green (light gray) line] as a function of the frustration f_x^{dc}. Here, we assume two resonators with center frequencies $f_A=3.5$ GHz and $f_B=3.5$ GHz+35 MHz. This corresponds to a relatively large center frequency spread[70] of 1%. In addition, we choose the two coupling coefficients $g_A/2\pi=472$ MHz and $g_B/2\pi=549$ MHz to differ by approximately 15%. It is remarkable that, also in this more general case, the switch setting condition can be fulfilled easily. We confirm this result by means of numerical simulations [solid blue (dark gray) line in Fig. 5] of the full Hamiltonian in Eq. (10), assuming fabrication imperfections. Interestingly, in contrast to the case where $\Delta_A=\Delta_B$ and $g_A=g_B$, we observe a different behavior of the analytical and numerical curves in Fig. 5 when moving far away from the qubit degeneracy point. The reasons behind this fact rely on the conditions used to obtain the

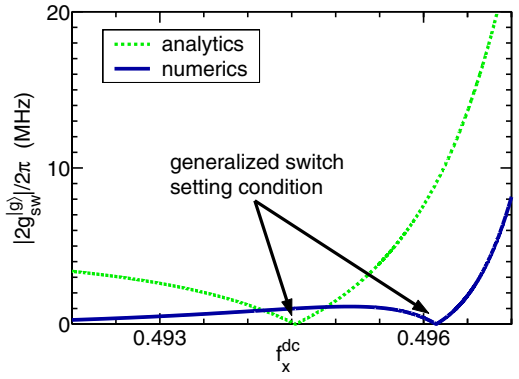

FIG. 5. (Color online) Robustness of the quantum against fabrication imperfections. Solid blue (dark gray) line: Numerical simulation of the quantum switch effective coupling coefficient $|2g_{sw}^{|g\rangle}|$ as a function of the frustration f_x^{dc}. Here, we assume a relatively large spread of 1% for the resonators' center frequencies (Ref. 70) and a difference of approximately 15% between g_A and g_B. Dashed green (light gray) line: Plot of $|2g_{sw}^{|g\rangle}|$ extracted from the generalized switch setting condition in Eq. (18) for the same parameter spread as in the numerical simulations. For both the analytical and the numerical results, the switch setting condition is fulfilled (see black arrows).

second-order Hamiltonian in Eq. (17). If $\delta_{AB} \gtrsim \max\{g_A g_B \sin^2 \theta/2\Delta_A, g_A g_B \sin^2 \theta/2\Delta_B, g_{AB}\}$, as for the parameters chosen here, this Hamiltonian does not represent an accurate approximation anymore. In this case, as expected, only partial agreement between analytics and numerics is found. Nevertheless, a clear switch setting condition is obtained in both cases. We notice that the numerical switch setting condition is shifted toward the degeneracy point with respect to the analytical solution. This is due to the detuning δ_{AB} present in Eq. (17), which is not accounted for when plotting the analytical solution. All the above considerations clearly show that the requirements on the sample fabrication are substantially relaxed.

B. Quantum switch protocol

We now propose a possible switching protocol based on three steps and discuss two different variants to shift from the zero-coupling to a finite-coupling condition characterized by a coupling coefficient g_{sw}^{on}. It is important to stress that this protocol is independent of the specific implementation (capacitive or inductive) of the switch. For definiteness, we choose a quantum switch based on a flux qubit in the following:

(i) First, we initialize the qubit in the ground state $|g\rangle$.

(ii) Second, in order to fulfill the switch setting condition, we choose the appropriate detuning Δ by changing the quasistatic bias of the qubit. For the switch operation to be practical, we assume $\Delta=\Delta_1>0$. In this way, the sign of the coefficient in front of the $\hat{\sigma}_z$ operator in Eq. (14) remains positive and, as a consequence, the switch is off in the ground state $|g\rangle$, i.e., $g_{sw}^{|g\rangle}=0$.

(iii) Third, the state of the quantum switch can now be changed from off to on in two different ways, (a) or (b).

(a) *Population inversion*. The qubit is maintained at the bias point preset in (ii). Its population is then inverted from $|g\rangle$ to $|e\rangle$, e.g., applying a Rabi π pulse of duration t_π. Such a pulse effectively changes the switch to the on state, $g_{sw}^{|e\rangle}=2g_{AB}$. In this case, $g_{sw}^{on}=2g_{AB}$. Under these conditions, the two resonators are effectively coupled and the A-to-B transfer time is $t=\pi/2g_{sw}^{on}$, which also constitutes the required time scale for most of the operations to be discussed in Sec. III C.

(b) *Adiabatic-shift pulse*. We opportunely change the quasistatic bias of the qubit by applying an adiabatic-shift pulse.[58] In this way, the qubit transition frequency becomes effectively modified. As a consequence, the detuning Δ is changed from Δ_1 to Δ_2 such that $g_{sw}^{|g\rangle}=\tilde{g}_{sw}=g_{AB}-g^2 \sin^2 \theta/\Delta_2 \neq 0$. In other words, the geometric and dynamic coupling coefficients are not balanced against each other anymore and the switch is set to the on-state. In this case, $g_{sw}^{on}=\tilde{g}_{sw}$. The rise time t_{rise} of the shift pulse has to fulfill the condition[3,58] $2\pi/g_{sw}^{on} \gtrsim t_{rise} \gtrsim \max\{2\pi/\delta_Q, 2\pi/\omega\}$.

Variant (b) strongly benefits from the dependence of $\tilde{g}_{sw}$ on the external quasistatic bias of the qubit [see Figs. 3(c) and 3(d)]. We can distinguish between two possible regimes. The first regime is for a flux bias close to the qubit degeneracy point, where the qubit-resonator detuning is reduced and, thus, $\Delta_2<\Delta_1$. In this case, the dynamic contribution to $\tilde{g}_{sw}$ dominates over the geometric one. This enables us to achieve very large resonator-resonator coupling strengths, which is a highly desirable condition for fast quantum operations (e.g., cf. Sec. III C). The second regime is for a flux bias far away from the qubit degeneracy point, where the qubit-resonator detuning is increased and, thus, $\Delta_2>\Delta_1$. In this case, the geometric contribution to $\tilde{g}_{sw}$ dominates over the dynamic one. Since very far away from the qubit degeneracy point $\tilde{g}_{sw} \to |2g_{AB}|$ [cf. Sec. III A and Figs. 4(a) and 4(b)], operating the system in the second regime allows us to probe the pure geometric coupling between A and B. This would constitute a direct measurement of the geometric second-order coupling when $M_{AQ}M_{QB}/M_{QQ} \gg m$.

C. Advanced applications: Nonclassical states and entanglement

We now provide a few examples showing how the quantum switch architecture can be exploited to create nonclassical states of the microwave radiation as well as entanglement of the resonators and qubit degrees of freedom. In this subsection, when we discuss *the* qubit, we refer to the one used for the quantum switch operation. If the presence of another qubit is required, we refer to it as the auxiliary qubit.

1. Fock state transfer and entanglement between the resonators

First, we assume the quantum switch to be turned off, e.g., following the protocol outlined in Sec. III B with the qubit in the ground state $|g\rangle$. In addition, we assume resonator A to be initially prepared in a Fock state $|1\rangle_A$, while cavity B remains in the vacuum state $|0\rangle_B$. Following the lines of Ref. 7, for example, a Fock state $|1\rangle_A$ can be created in A by means of an auxiliary qubit coupled to it. A population inversion of the auxiliary qubit (via a π pulse) and its subsequent relaxation suffice to achieve this purpose. Then, we turn on the quan-

tum switch for a certain time t following either one of the two variants (a) or (b) introduced in Sec. III B. The initial states are $|e\rangle|1\rangle_A|0\rangle_B$ and $|g\rangle|1\rangle_A|0\rangle_B$ for (a) and (b), respectively. The quantum switch is now characterized by an effective coupling g_{sw}^{on} and the dynamics associated with the Hamiltonian in Eq. (14) is activated for the time t. In this manner, a coherent linear superposition of bipartite states containing a Fock state single photon[3,7,8,60,71] can be created,

$$\cos(g_{sw}^{on}t)|1\rangle_A|0\rangle_B + e^{j\pi/2}\sin(g_{sw}^{on}t)|0\rangle_A|1\rangle_B, \tag{19}$$

where the qubit state does not change and qubit and resonators remain disentangled. If we choose to wait for a time $t=\pi/2g_{sw}^{on}$, we can exploit Eq. (19) as a mechanism for the transferring of a Fock state from resonator A to resonator B, $|1\rangle_A|0\rangle_B \rightarrow |0\rangle_A|1\rangle_B$. In this case, the resonators also remain disentangled. It is worth mentioning that the controlled transfer of a Fock state between two remote locations constitutes the basis of several quantum information devices.[72] If we choose to wait for a time $t=\pi/4g_{sw}^{on}$ instead, we can achieve maximal entanglement between the two remote resonators. This goes beyond the results obtained in atomic systems, where two nondegenerate orthogonally polarized modes of the same cavity have been used to create mode entanglement.[30]

2. Tripartite entanglement and Greenberger-Horne-Zeilinger states

We follow a modified version of variant (a) of the switching protocol. We start from the same initial conditions as in the previous example. Resonator A is in $|1\rangle_A$ and resonator B is in $|0\rangle_B$. The qubit is in $|g\rangle$ and the switch setting condition is fulfilled; i.e., the switch is off. We then apply a $\pi/2$ pulse to the qubit, bringing it into the symmetric superposition[73] $(|g\rangle+|e\rangle)/\sqrt{2}$. Then, the state of the system is still disentangled and can be written as

$$\frac{|g\rangle|1\rangle_A|0\rangle_B + |e\rangle|1\rangle_A|0\rangle_B}{\sqrt{2}}. \tag{20}$$

Now, the Hamiltonian in Eq. (14) yields the time evolution

$$\frac{1}{\sqrt{2}}\Big[|g\rangle|1\rangle_A|0\rangle_B + \cos(g_{sw}^{on}t)|e\rangle|1\rangle_A|0\rangle_B + e^{j\pi/2}\sin(g_{sw}^{on}t)|e\rangle|0\rangle_A|1\rangle_B\Big] \tag{21}$$

for the state of the quantum switch. Under these conditions, the dynamics displayed in Eq. (21) is characterized by two distinct processes. The first one acts on the $|g\rangle|1\rangle_A|0\rangle_B$ part of the initial state of Eq. (20). This process is actually frozen because the quantum switch is turned off when the qubit is in $|g\rangle$. The second process, instead, acts on the $|e\rangle|1\rangle_A|0\rangle_B$ part of the initial state, starting the transfer of a single photon from resonator A to resonator B and vice versa. If during such evolution we wait for a time $t=\pi/2g_{sw}^{on}$, a tripartite entangled state

$$\frac{|g\rangle|1\rangle_A|0\rangle_B + e^{j\pi/2}|e\rangle|0\rangle_A|1\rangle_B}{\sqrt{2}} \tag{22}$$

of the Greenberger-Horne-Zeilinger (GHZ) class[74] is generated. Here, the two resonators can be interpreted as photonic qubits because only the Fock states $|0\rangle_{A,B}$ and $|1\rangle_{A,B}$ are involved. Hence, Eq. (22) represents a state containing maximal entanglement for a three-qubit system, which consists of two photonic qubits and one superconducting (charge or flux) qubit. The generation of GHZ states is important for the study of the properties of genuine multipartite entanglement. Interestingly, the quantum nature of our switch is embodied in the linear superposition of $|g\rangle|1\rangle_A|0\rangle_B$ and $|e\rangle|1\rangle_A|0\rangle_B$ of the initial state of Eq. (20).

3. Entanglement of coherent states

Finally, we show how to produce entangled coherent states of the intracavity microwave fields of the two resonators. These are prototypical examples of the vast class of states referred to as Schrödinger cat states.[21,43,75–77] This time, we start with cavity A populated by a coherent state $|\alpha\rangle_A$ instead of a Fock state $|1\rangle_A$. Again, cavity B is in the vacuum state $|0\rangle_B$ and the qubit in the symmetric superposition state $(|g\rangle+|e\rangle)/\sqrt{2}$, i.e., a modified version of variant (a) of the switching protocol is one more time employed. The total disentangled initial state can be written as

$$\frac{|g\rangle|\alpha\rangle_A|0\rangle_B + |e\rangle|\alpha\rangle_A|0\rangle_B}{\sqrt{2}}. \tag{23}$$

The resulting dynamics associated with the Hamiltonian in Eq. (14) yields a time evolution similar to that shown for Fock states in Eq. (21). In this case, the part of the evolution involving $|e\rangle$ can be calculated either quantum mechanically or by employing a semiclassical model. In both cases, after a waiting time $t=\pi/2g_{sw}^{on}$, resonator B is in the state $|\alpha\rangle_B$ and A is in the vacuum state $|0\rangle_A$. However, Eq. (23) contains an initial linear superposition of $|g\rangle|\alpha\rangle_A|0\rangle_B$ and $|e\rangle|\alpha\rangle_A|0\rangle_B$, requiring a quantum-mechanical treatment of the time evolution. From this, one finds that after the waiting time $t=\pi/2g_{sw}^{on}$, the quantum switch operation creates the tripartite GHZ-type entangled state

$$\frac{|g\rangle|\alpha\rangle_A|0\rangle_B + e^{j\varphi}|e\rangle|0\rangle_A|\alpha\rangle_B}{\sqrt{2}}, \tag{24}$$

where φ is an arbitrary phase. Again, the creation of such states clearly reveals the quantum nature of our switch, showing a departure from standard classical switches.[57] Remarkably, the state of Eq. (24) describes the entanglement of coherent ("classical") states in both resonators. This feature is peculiar to our quantum switch and cannot easily be reproduced in atomic systems.[30] In principle, in the absence of dissipation the quantum switch dynamics continues transferring back the coherent state to cavity A. In order to stop this evolution, an ultimate measurement of the qubit along the x axis of the Bloch sphere[7,78] is necessary. This corresponds to a projection associated with the Pauli operator $\hat{\sigma}_x$, which creates the two-resonator entangled state

$$\frac{|\alpha\rangle_A|0\rangle_B + e^{j\varphi}|0\rangle_A|\alpha\rangle_B}{\sqrt{2}}. \quad (25)$$

This state is decoupled from the qubit degree of freedom.

Obviously, all the protocols discussed above need suitable measurement schemes to be implemented in reality. For instance, it is desirable to measure the transmitted microwave field through both resonators and, eventually, opportune cross correlations between them by means of a double heterodyne detection apparatus similar to that in Ref. 60. In addition, a direct measurement of the qubit state, e.g., by means of a dc SQUID coupled to it[3,12] would allow for the full characterization of the quantum switch device. In summary, we show that a rich landscape of nonclassical and multipartite entangled states can be created and measured by means of our quantum switch in two-resonator circuit QED.

IV. TREATMENT OF DECOHERENCE

The discussion in Secs. II and III implicitly assumes pure quantum states. In reality, however, a quantum system gradually decays into an incoherent mixed state during its time evolution. This process, called decoherence, is due to the entanglement of the system with its environment and it is known to be a critical issue for solid-state quantum circuits. Since it is difficult to decouple these circuits from the large number of environmental degrees of freedom to which they are exposed, their typical decoherence rates cannot easily be minimized. Usually, they are in the range from 1 MHz to 1 GHz, depending on the specific implementation. In this section, we discuss the impact of the three most relevant decoherence mechanisms on the quantum switch architecture. These are, first, the population decay of resonators A and B with rates κ_A and κ_B, respectively; second, the qubit relaxation from the energy excited state to the ground state at a rate γ_r due to high-frequency noise; and third, the qubit dephasing (loss of phase coherence) at a pure dephasing rate γ_φ due to low-frequency noise. We show by means of detailed analytical derivations that, despite decoherence mechanisms, a working quantum switch can be realized with readily available superconducting qubits and resonators.

Decoherence processes are most naturally described in the qubit energy eigenbasis $\{|g\rangle,|e\rangle\}$. Under the Markov approximation, the time evolution of the density matrix of the quantum switch Hamiltonian $\hat{H}$ in Eq. (11) is described by the master equation

$$\dot{\hat{\rho}} = \frac{1}{j\hbar}(\hat{H}\hat{\rho} - \hat{\rho}\hat{H}) + \sum_{n=1}^{4} \hat{\mathcal{L}}_n\hat{\rho}. \quad (26)$$

Here, $\dot{\hat{\rho}} \equiv (\partial/\partial t)\hat{\rho}$ and $\hat{\mathcal{L}}_n$ is the Lindblad superoperator defined as $\hat{\mathcal{L}}_n\hat{\rho} \equiv \gamma_n(\hat{X}_n\hat{\rho}\hat{X}_n^\dagger - \hat{X}_n^\dagger\hat{X}_n\hat{\rho}/2 - \hat{\rho}\hat{X}_n^\dagger\hat{X}_n/2)$. The indices $n=1,2,3,4$ label the decay of resonator A, the decay of resonator B, qubit relaxation, and qubit dephasing, respectively. Consequently, the generating operators are $\hat{X}_1 \equiv \hat{a}$, $\hat{X}_1^\dagger \equiv \hat{a}^\dagger$, $\hat{X}_2 \equiv \hat{b}$, $\hat{X}_2^\dagger \equiv \hat{b}^\dagger$, $\hat{X}_3 \equiv \hat{\sigma}^-$, $\hat{X}_3^\dagger \equiv \hat{\sigma}^+$, and $\hat{X}_4 = \hat{X}_4^\dagger \equiv \hat{\sigma}_z$. The corresponding decoherence rates are $\gamma_1 \equiv \kappa_A$, $\gamma_2 \equiv \kappa_B$, $\gamma_3 \equiv \gamma_r$, and $\gamma_4 \equiv \gamma_\varphi/2$. For the resonators, κ_A and κ_B are often expressed in terms of the corresponding loaded quality factors Q_A and Q_B, $\kappa_A \equiv \omega_A/Q_A$ and $\kappa_B \equiv \omega_B/Q_B$, respectively. Although in general all four processes coexist, in most experimental situations one of them dominates over the others. In fact, it is a common experimental scenario that $\gamma_\varphi \gg \gamma_r$, for example in the special case of a flux qubit operated away from the degeneracy point (see, e.g., Ref. 58). In this situation, we can extract pessimistic relaxation and dephasing rates from the literature,[58,79–81] $\gamma_r \simeq 1$ MHz and $\gamma_\varphi \simeq 200$ MHz. In other words, dephasing is the dominating source of qubit decoherence.[82] The decay rates of the resonators can be engineered such that[70] $\kappa_A, \kappa_B \lesssim \gamma_r \ll \gamma_\varphi$. For these reasons, hereafter we focus on dephasing mechanisms only. Hence, we analyze the following simplified master equation:

$$\dot{\hat{\rho}} = \frac{1}{j\hbar}(\hat{H}\hat{\rho} - \hat{\rho}\hat{H}) + \hat{\mathcal{L}}_\varphi\hat{\rho}, \quad (27)$$

where $\hat{\mathcal{L}}_\varphi\hat{\rho} \equiv \hat{\mathcal{L}}_4\hat{\rho} = (\gamma_\varphi/2)(\sigma_z\hat{\rho}\hat{\sigma}_z - \hat{\rho})$.

The impact of qubit dephasing on the switch operation depends on the chosen protocol (cf. Sec. III B). When employing the population-inversion protocol, qubit dephasing occurs within the duration time t_π of the control π pulses. The time t_π coincides with the inverse of the qubit Rabi frequency and can be reduced to less than 1 ns using high driving power.[83] In this way, the time window during which the qubit is sensitive to dephasing is substantially shortened. However, it is more favorable to resort to the adiabatic-shift pulse protocol. In this case, the qubit always remains in $|g\rangle$, resulting in a complete elimination of pulse-induced dephasing. The relevant time scale during which dephasing occurs is therefore set by the operation time of the switch between two on-off events. Naturally, this time should be as long as possible if we want to perform many operations.

The effect of dephasing during the switch operation time is better understood by inspecting the effective quantum switch Hamiltonian $\hat{H}_{\text{eff}}$ in Eq. (14). In Sec. III A, we deduce this effective Hamiltonian by means of a Dyson series expansion. This approach is very powerful and compact when dealing with the analysis of a unitary evolution. However, when treating master equations, we prefer to utilize a variant of the well-known Schrieffer-Wolff unitary transformation,[22,84] $\hat{U}\hat{H}\hat{U}^\dagger$, where

$$\hat{U} \equiv \exp\left[\frac{g_A \sin\theta}{\Delta}(\hat{\sigma}^-\hat{a}^\dagger - \hat{\sigma}^+\hat{a}) + \frac{g_B \sin\theta}{\Delta}(\hat{\sigma}^-\hat{b}^\dagger - \hat{\sigma}^+\hat{b})\right] \quad (28)$$

and $\hat{U}^\dagger$ is its Hermitian conjugate. In the large-detuning regime, $g_A \sin\theta$, $g_B \sin\theta \ll \Delta$, we can neglect all terms of orders $(g_A \sin\theta/\Delta)^2$, $(g_B \sin\theta/\Delta)^2$, $g_A g_B \sin^2\theta/\Delta^2$, or higher. After a transformation into an interaction picture with respect to the qubit and both resonators (cf. Sec. III A) and performing opportune RWAs, we obtain again $\hat{H}_{\text{eff}}$ of Eq. (14). The master equation governing the time evolution of the effective density matrix $\hat{\rho}^{\text{eff}} \equiv \hat{U}\hat{\rho}\hat{U}^\dagger$ then becomes

$$\dot{\hat{\rho}}^{\text{eff}} = \frac{1}{j\hbar}(\hat{H}_{\text{eff}}\hat{\rho}^{\text{eff}} - \hat{\rho}^{\text{eff}}\hat{H}_{\text{eff}}) + \hat{\mathcal{L}}_{\varphi}^{\text{eff}}\hat{\rho}^{\text{eff}}. \tag{29}$$

The analysis is complicated by the fact that also the Lindblad superoperator $\hat{\mathcal{L}}\hat{\rho}$ has to be transformed. For the sake of simplicity, we can assume $g_A = g_B \equiv g$ and find

$$\hat{\mathcal{L}}_{\varphi}^{\text{eff}}\hat{\rho}^{\text{eff}} \approx \hat{\mathcal{L}}_{\varphi}\hat{\rho}^{\text{eff}} + 2\gamma_{\varphi} \times \mathcal{O}\left[\left(\frac{g \sin\theta}{\Delta}\right)^2\right]. \tag{30}$$

When deriving this expression, all terms of $\mathcal{O}(g \sin\theta/\Delta)$ are explicitly neglected by a RWA. This approximation relies on the condition $(\gamma_{\varphi}/\Delta)g \sin\theta \ll \Delta$, which is well satisfied in the large-detuning regime as long as $\gamma_{\varphi} \lesssim \Delta$. The latter requirement can easily be met by most types of existing superconducting qubits. In the frame of $\hat{H}_{\text{eff}}$, $\hat{\mathcal{L}}_{\varphi}\hat{\rho}^{\text{eff}}$ has the standard Lindblad dephasing structure and the qubit appears only in the form of $\hat{\sigma}_z$ operators. Since the initial state of the switch operation is characterized by either no (adiabatic-shift pulse protocol) or only very small (population-inversion protocol) qubit coherences, the effect of $\hat{\mathcal{L}}_{\varphi}\hat{\rho}^{\text{eff}}$ on the time evolution of the system is negligible. All other nonvanishing terms are comprised in the expression $2\gamma_{\varphi} \times \mathcal{O}[(g \sin\theta/\Delta)^2]$ in Eq. (30) and scale with a factor smaller than $\gamma_{\varphi}^{\text{eff}} \equiv 2\gamma_{\varphi}(g \sin\theta/\Delta)^2$. Hence, the operation of the quantum switch is robust against qubit dephasing on a characteristic time scale $T_{\varphi}^{\text{eff}} = 1/\gamma_{\varphi}^{\text{eff}} \gg 1/\gamma_{\varphi}$. For completeness, it is important to mention that the higher-order terms in Eq. (30) can contain combinations of operators such as $\hat{a}^{\dagger}\hat{a}$ and $\hat{b}^{\dagger}\hat{b}$. In this case, T_{φ}^{eff} would be reduced for a large number of photons populating the resonators. Fortunately, this does not constitute a major issue since the most interesting applications of a quantum switch require that the number of photons in the resonators is on the order of 1.

In summary, we show that for suitably engineered cavities the quantum switch operation time for the adiabatic-shift pulse protocol is limited only by the effective qubit dephasing time T_{φ}^{eff}. The latter is strongly enhanced with respect to the intrinsic dephasing time $T_{\varphi} \equiv 1/\gamma_{\varphi}$. In this sense, the quantum switch is superior to the dual setup, where two qubits are dispersively coupled via one cavity bus.[6] Moreover, the intrinsic dephasing time T_{φ} and, consequently, T_{φ}^{eff} are further enhanced by choosing a shift pulse which sets the on-state bias near the qubit degeneracy point.[58] As explained in Sec. III B, this regime takes place for a qubit-resonator detuning $\Delta_2 < \Delta_1$. In this case, the switch coupling coefficient is also substantially increased because of a dominating dynamic interaction. As a consequence, this option is particularly appealing in the context of the advanced applications discussed in Sec. III C. Finally, we notice that for the population-inversion protocol, the switch operation time could be limited by the qubit relaxation time $T_r \equiv 1/\gamma_r$. However, the switch setting condition is typically fulfilled for a bias away from the qubit degeneracy point. There, T_r is considerably enhanced by both a reduced[58] $\sin\theta$ and the Purcell effect of the cavities.[22]

V. EXAMPLE OF TWO-RESONATOR CIRCUIT QED WITH A FLUX QUBIT

In this section, we focus on the geometry sketched in Fig. 1(c) and present one specific implementation of two-resonator circuit QED. As a particular case, the described setup can be operated as a superconducting quantum switch. In this example, we consider microstrip resonators. Coplanar waveguide resonators can also be used without significantly affecting our main results. In addition, we choose a flux qubit because this is our main topic of research.[12,58,60,81] Moreover, as shown in Sec. III A, the dynamic properties of the quantum switch are independent of specific implementations. As a consequence, in this section we concentrate on its geometric properties only. It is worth mentioning again that such properties are inherent to circuit QED architectures and constitute a fundamental departure from quantum-optical systems.

In Figs. 6(a) and 6(b), the design of a possible two-resonator circuit QED setup is shown. The overall structure is composed of two superconducting microstrip transmission lines, which are bounded by input and output capacitors, $C_{a,in}$, $C_{b,in}$, $C_{a,out}$, and $C_{b,out}$. This geometrical configuration forms the two resonators A and B. The input and output capacitors also determine the loaded or external quality factors Q_A and Q_B of the two resonators.[85] Both A and B are characterized by a length ℓ_m, which defines their center frequencies f_A and f_B. We choose $\ell_m = \lambda_m/2 = 12$ mm, where $\lambda_m \equiv \lambda_A = \lambda_B$ is the full wavelength of the standing waves on the resonators. The superconducting loop of the flux qubit circuit is positioned at the current antinode of the two $\lambda_m/2$ resonators.

In Fig. 6(c), only the two microstrip resonators A and B are considered. They are chosen to have a width $W_m = 10$ μm and a thickness $t_m = 100$ nm. The height of the dielectric substrate between each microstrip and the corresponding ground plane is $H_s = 12.3$ μm. The substrate can opportunely be made of different materials, such as, for example, silicon, sapphire, amorphous hydrogenated silicon, or silicon oxide, depending on the experimental necessities. A detailed study on the properties of a variety of dielectrics and on the dissipation processes of superconducting on-chip resonators can be found in Refs. 86–90. The aspect ratio W_m/H_s is engineered to guarantee a line characteristic impedance $Z_c \simeq 50$ Ω, even if this is not a strict requirement for the resonators to function properly.[91] The remaining dimensions of our system are shown in Fig. 6(b): The lateral dimensions $\ell_{q1} = 200$ μm and $\ell_{q2} = 87$ μm of the qubit loop, the width $W_q = 1$ μm of each line forming the qubit loop, the interspace $d_{mq} = 1$ μm between qubit and resonators, and the thickness $t_q (= t_m) = 100$ nm of the qubit lines. The dimensions of the qubit loop are chosen to optimize the qubit-resonator coupling strengths. This geometry results in a relatively large inductance $L_q \simeq 780$ pH (number obtained from FASTHENRY simulations;[92] cf. Table I). Despite the large self-inductance L_q, reasonable qubit coherence times are expected (see, e.g., Refs. 25 and 93). Moreover, in light of Sec. IV these coherence times easily suffice for the operation of a superconducting quantum switch, where the qubit acts as a mere mediator for the exchange of virtual excitations.

In our numerical simulations (cf. Appendix B), we restrict ourselves to the region indicated by the black dashed box in

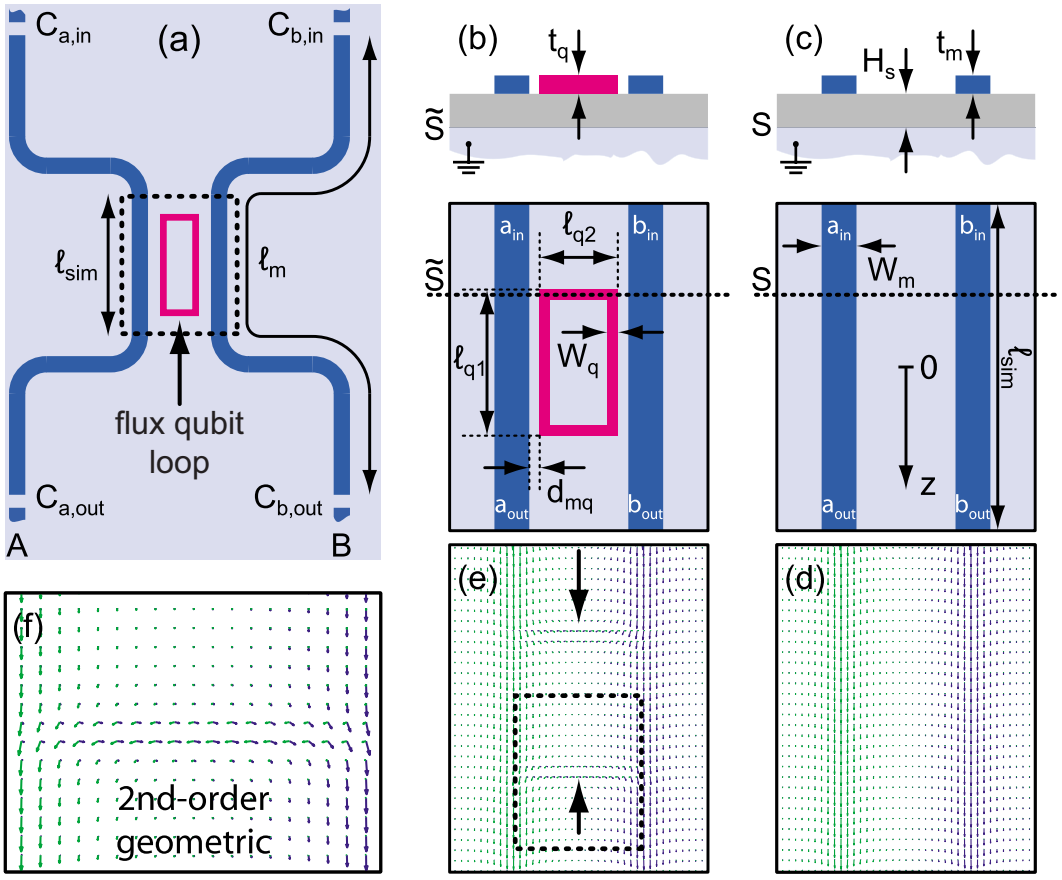

FIG. 6. (Color online) A possible setup for two-resonator circuit QED with a flux qubit. (a) Overall structure (dimensions not in scale). Two microstrip resonators A and B (thick blue lines) of length ℓ_m simultaneously coupled to a flux qubit loop [magenta (middle gray) rectangle]. $C_{a,in}$, $C_{b,in}$, $C_{a,out}$, and $C_{b,out}$: Input and output capacitors for A and B. The dashed black box indicates the region of the closeup shown in (b). ℓ_{sim}: Length of the region used for the FASTHENRY (Ref. 92) simulations. (b) Closeup of the region which contains the flux qubit loop in (a). ℓ_{q1} and ℓ_{q2}: Qubit loop lateral dimensions. W_q: Width of the qubit lines. d_{mq}: Distance between the qubit and each resonator. The dashed black line denoted as $\tilde{S}$ marks the cross section reported on the top part of the panel. t_q: Thickness of the qubit loop lines. (c) Same as (b) but without the qubit loop. W_m and t_m: Width and thickness (see cross section S) of the two microstrip resonators. H_s: Height of the dielectric substrate. The reference axis $0z$ is also indicated (cf. Appendix B). Both in (b) and (c), a_{in}, a_{out}, b_{in}, and b_{out} represent the input and output probing ports used in the simulations. (d) Current-density distribution at high frequency (5 GHz) for the structures drawn in (c). The currents are represented by small arrows, green (light gray) for resonator A and blue (dark gray) for resonator B. (e) Current-density distribution at high frequency (5 GHz) for the structures drawn in (b). The two black arrows indicate two high-current-density channels between the two resonators. The dashed black box marks the close-up area shown in (f). (f) Closeup of one of the two geometric second-order interaction channels.

Fig. 6(a), closeups of which are shown in Fig. 6(b) and, in the absence of the flux qubit loop, in Fig. 6(c). This region is characterized by a length $\ell_{sim}=500$ μm of the resonators and is centered at a position where the magnetic field reaches a maximum (antinode) and the electric field reaches a minimum (node). We notice that magnetic and electric fields can equivalently be expressed in terms of currents and voltages, respectively. There are two main hypotheses behind the validity of our simulation results for the entire two-resonator-qubit system. These are the uniformity of the electromagnetic field (voltage and current) in the simulated region and the abruptly[94] increasing geometric distance between resonators A and B outside of it [see sketch in Fig. 6(a)]. The three main implications of the above assumptions are explained in the following: First, all coupling strengths are dominated by inductive interactions and there are no appreciable capacitive ones. Inside the simulated region, in fact, the voltage is practically characterized by a node, which results in a vanishing coupling coefficient. Outside the simulated region, the effective distance d_{eff} between the cavities strongly increases together with the geometric one.[95,96] As a consequence, the geometric first-order capacitance $c \propto 1/d_{eff}$ becomes negligible. Second, the coupling coefficients between qubit and resonators can be obtained without integrating over the spatial distribution of the mode. This is because of the uniformity of the field, which, for all practical purposes, is constant over the restricted simulated region. Third, the geometric first-order coupling between the two resonators, which is proportional to their mutual inductance m, is still accurately determined. In fact, outside the simulated region any additional contribution to m becomes negligible. For all the reasons mentioned above, we are allowed to use the FASTHENRY

(Ref. 92) calculation software for our simulations. In this section, we utilize two different versions of FASTHENRY, one for superconducting materials and one for almost perfectly conducting ones. We use the second version only when we want to obtain current-density distributions or the frequency dependence of an inductance. In these cases, due to the technical limitations of the software, we cannot use the version valid for superconductors.[92]

Figures 6(d) and 6(e) display the simulated current-density distributions at a probing frequency of 5 GHz (high-frequency regime) for the different structures drawn in Figs. 6(c) and 6(b), respectively. Similar results can be found in a range between 1 and 10 GHz (data not shown). Without loss of generality, these simulations are performed for almost perfect conductors using a FASTHENRY version which does not support superconductivity. The results in Fig. 6(d) clearly show that the two microstrip lines correspond to regions characterized by a high current density separated by a region with a low current density in the absence of the flux qubit loop. In this case, the geometric interaction between resonators A and B is reduced to a bare first-order coupling, which turns out to be very weak. On the contrary, in Fig. 6(e) the presence of the qubit loop clearly opens two new current channels between A and B. These are located at the positions of the upper and lower qubit loop segments in Fig. 6(b). For clarity, the closeup of one of these channels is shown in Fig. 6(f). Notably, the two additional current channels in Fig. 6(e) represent the geometric second-order coupling.

We now study in detail the relationship between first- and second-order inductances for the structures in Figs. 6(b) and 6(c). The notation is that of Sec. II C and Figs. 2(d)–2(f). All quantities are computed numerically with the aid of FASTHENRY for superconducting materials[92] assuming a London penetration depth $\lambda_L=180$ nm. We notice that in this case, the simulated inductances are independent of the probing frequency. In a first run of simulations, we calculate pure first-order inductances only (cf. Appendix B). These are the simulated test inductances L_{ra}^* and L_{rb}^* from which we obtain the self-inductances L_{ra} and L_{rb} of resonators A and B (more details in the next paragraph), the first-order mutual inductance m between the two resonators, the self-inductance L_q of the qubit loop, and the mutual inductances M_{qa} and M_{qb} between qubit and resonators. In a second run of simulations, we calculate directly (cf. Appendix B) the sum of first- and second-order inductances. These are the renormalized test inductances $\tilde{L}_{ra}^*$ and $\tilde{L}_{rb}^*$ of the portions of resonators A and B shown in Fig. 6(b) and the total mutual inductance $\tilde{m}$ between the two resonators. The difference $\tilde{m}-m=4.781\,92$ pH, i.e., the geometric second-order coupling, coincides up to the sixth significant digit with the quantity $M_{qa}M_{qb}/L_q$ expected from our general three-node network approach in Sec. II B and, equivalently, from the three-circuit theory in Sec. II C (cf. Table I). We also find that the dominating geometric coupling between A and B is not the first-order inductance $m=2.901\,30$ pH but the second-order one. The ratio between second-order and first-order inductances is $(\tilde{m}-m)/m \simeq 1.6$. In addition, the numerical simulations yield the two shift test inductances $|\tilde{L}_{ra}^*-L_{ra}^*|=|\tilde{L}_{rb}^*-L_{rb}^*|=4.781\,00$ pH (cf. also next paragraph). These shifts renormalize the bare center frequencies f_A and f_B of resonators A and B, respectively, and are found to be in very good agreement up to several decimal digits with their analytical estimates $L_{sa}\equiv M_{qa}^2/L_q$ and $L_{sb}\equiv M_{qb}^2/L_q$ of our three-circuit theory in Sec. II C (cf. Table I). We point out that in our definition, the quantities L_{sa} and L_{sb} are strictly positive. Remarkably, our simulations reveal that $L_{ra}^*>\tilde{L}_{ra}^*$ and $L_{rb}^*>\tilde{L}_{rb}^*$, reproducing the minus sign in the expressions $L_{ra}-L_{sa}$ and $L_{rb}-L_{sb}$ in Fig. 2(f). These findings confirm the superiority of the three-circuit theory in Sec. II C over the simple model which results in the Hamiltonian of Eq. (9). In the case of purely inductive interactions, the resonators suffer a small blueshift of their center frequencies, i.e., a shift toward higher values. This is opposite to the redshift, i.e., toward lower frequencies, experienced by the resonators for a pure capacitive coupling [cf. Sec. II C and Fig. 2(c)].

The numerical values of all parameters discussed above are listed in Table I. The values of the bare self-inductances of the two resonators are first evaluated for the test length ℓ_{sim} in the absence of the qubit loop. This yields the simulated test inductances L_{ra}^* and L_{rb}^*. Then, L_{ra}^* and L_{rb}^* are extrapolated to the full length ℓ_m of each microstrip resonator to obtain L_{ra} and L_{rb}, respectively. In the presence of the qubit loop, the simulated test inductances $\tilde{L}_{ra}^*$ and $\tilde{L}_{rb}^*$ can also be found. The resonator capacitances per unit length, c_{ra} and c_{rb}, are calculated analytically by means of a conformal mapping technique:[95]

$$c_{ra}=c_{rb}=2\pi\epsilon_0\epsilon_r \ln\left(\frac{8H_s}{W_m^{\mathrm{eff}}}+\frac{W_m^{\mathrm{eff}}}{4H_s}\right). \tag{31}$$

Here, $\epsilon_0=8.854\times10^{-12}$ F/m is the permittivity of vacuum (electric constant),[97] $\epsilon_r=11.5$ is the relative dielectric constant of the substrate (in our example, sapphire or silicon; other dielectrics could be used), and $W_m^{\mathrm{eff}}\equiv W_m+0.398t_m[1+\ln(2H_s/t_m)]$ is the effective width of the resonators.[95] As a consequence, the resonator capacitances are $C_{ra}=\ell_m c_{ra}$ and $C_{rb}=\ell_m c_{rb}$. Finally, from the knowledge of the velocity of the electromagnetic waves inside the two resonators, $\bar{c}_A\equiv\ell_m/\sqrt{(L_{ra}C_{ra})}$ and $\bar{c}_B\equiv\ell_m/\sqrt{(L_{rb}C_{rb})}$, one can find the full wavelengths $\lambda_A=\bar{c}_A/f_A$ and $\lambda_B=\bar{c}_B/f_B$ of the two resonators. As before, all these results are summarized in Table I.

We now analyze the frequency dependence of the geometric first- and second-order coupling coefficients, i.e., the first- and second-order mutual inductances, for a broad frequency span between 1 Hz and 10 GHz. Again, we assume almost perfectly conducting structures and use the FASTHENRY version which does not support superconductivity. The results are plotted in Figs. 7 and 8. In Fig. 7(a), we plot the frequency dependence of the simulated inductances L_q (which is renormalized by a factor of 8.5 for clarity) and $M_{qa}=M_{qb}$. From these, we then compute the expression $M_{qa}M_{qb}/L_q$ for the second-order mutual inductance as derived in Secs. II B and II C. This expression is plotted in Fig. 7(b). In Fig. 7(c), we plot the bare second-order mutual inductance $\tilde{m}-m$ as a function of frequency. Remarkably, comparing Fig. 7(b) to Fig. 7(c), we find $M_{qa}M_{qb}/L_q=\tilde{m}-m$ with very high accuracy over the entire frequency range. In the frequency region of interest for the operation of a quantum switch, i.e., from

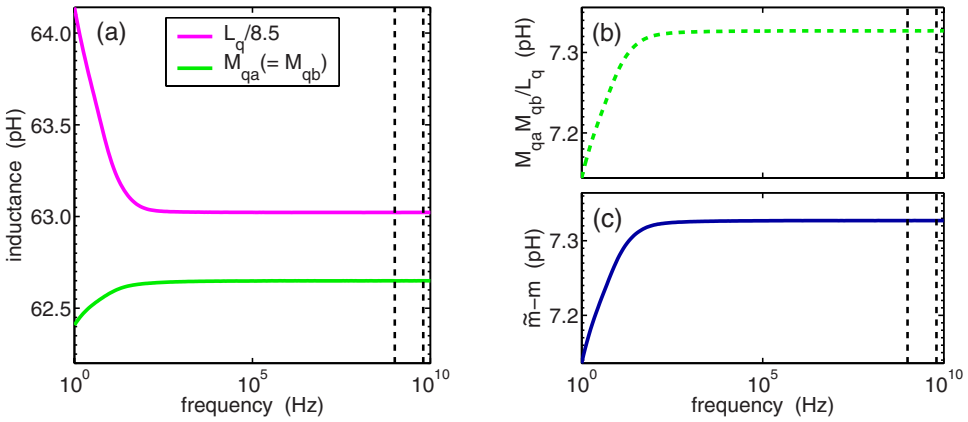

FIG. 7. (Color online) FASTHENRY simulation results for the frequency dependence of some relevant first- and second-order inductances important for our example of two-resonator circuit QED. Vertical dashed black lines: Frequency region of interest for the operation of the quantum switch from 1 to 6 GHz. (a) Magenta (middle gray) line: Qubit loop self-inductance L_q renormalized by a factor of 8.5 for clarity. Green (light gray) line: Mutual inductance M_{qa} $(=M_{qb})$ between the qubit and resonator A (or B). (b) Bare second-order mutual inductance between the two resonators calculated with the results from (a) using the expression $M_{qa}M_{qb}/L_q$. (c) Bare second-order mutual inductance between the two resonators $\tilde{m}-m$. The agreement with (b) is excellent.

approximately 1 to 6 GHz, we find $L_q \simeq 63.02$ pH, $M_{qa}=M_{qb}\simeq 7.37$ pH, and, consequently, $M_{qa}M_{qb}/L_q=\tilde{m}-m \simeq 7.33$ pH. All these results prove again the general validity of the derivations in Secs. II B and II C.

Finally, we study the scattering matrix elements between resonators A and B both without and with flux qubit loop. In absolute value, these elements correspond to the isolation coefficients between A and B. As before, the FASTHENRY simulations are performed within the regions in Figs. 6(c) and 6(b). In these figures, we also define the input and output probing ports used in the simulations as a_{in} and b_{in} and a_{out} and b_{out}, respectively. Under these assumptions, the scattering matrix element $S_{ab}=S_{ba}$ in the absence of the flux qubit loop is given by[95,96]

$$S_{ab} \equiv 20 \log \left| \frac{-I^-_{a_{in}}}{I^+_{b_{in}}} \right|_{I^+=0} = 20 \log \frac{m}{L^*_{ra}}, \tag{32}$$

where $I^+_{b_{in}}$ is a test current wave incident on the input probing port b_{in} of resonator B. The current $-I^-_{a_{in}}$ corresponds to the outgoing wave from the input probing port a_{in} of resonator A. The remaining current waves incident on the ports of the two resonators are $I^+ \equiv \{I^+_{a_{in}}, I^+_{a_{out}}, I^+_{b_{out}}\}$. In a similar way, the scattering matrix element $\tilde{S}_{ab}=\tilde{S}_{ba}$ in the presence of the flux qubit loop is given by

$$\tilde{S}_{ab} = 20 \log \frac{\tilde{m}}{\tilde{L}^*_{ra}}. \tag{33}$$

We note that the same results as in Eqs. (32) and (33) are obtained after replacing the input probing port b_{in} with the output probing port b_{out} for the incident wave. In this case, the associated current $I^+_{b_{in}}$ has to be exchanged with $I^+_{b_{out}}$. Similar substitutions apply for the probing port and associated current of the outgoing waves. In the literature,[95] the outgoing waves are often denominated as reflected waves. Equation (32) can be straightforwardly found via the definitions of mutual inductance and self-inductance, $mI^+_{b_{in}}=\Phi_{ba}=L^*_{ra}I^-_{a_{in}}$. There, Φ_{ba} is the flux generated in the portion of resonator A by the current flowing in the portion of resonator B in Fig. 6(c). Similar arguments lead to Eq. (33). When considering superconducting materials, the scattering matrix elements between A and B without and with flux qubit loop can be evaluated by inserting the opportune numbers reported in Table I into Eqs. (32) and (33). This yields $S_{ab}\simeq -38.80$ dB and $\tilde{S}_{ab}\simeq -30.18$ dB. If we want to calculate the scattering matrix elements between A and B over a broad frequency span (e.g., from 1 Hz to 10 GHz), we can consider again almost perfectly conducting structures. In this case, the results are plotted in Figs. 8(a) and 8(b). In the high-

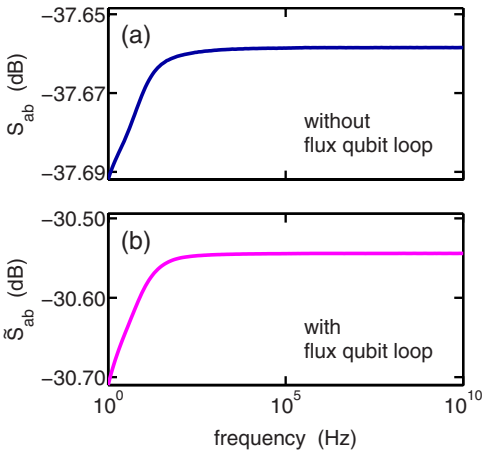

FIG. 8. (Color online) FASTHENRY simulation results for the frequency dependence of the scattering matrix elements between resonators A and B considering almost perfectly conducting structures. Frequency span: From 1 Hz to 10 GHz. (a) Scattering matrix element S_{ab} in the absence of the flux qubit loop. (b) Scattering matrix element $\tilde{S}_{ab}$ in the presence of the flux qubit loop. Owing to the significant second-order mutual inductance between A and B, we find $|\tilde{S}_{ab}|<|S_{ab}|$.

frequency region from 1 to 6 GHz, we find $S_{ab} \simeq -37.66$ dB and $\tilde{S}_{ab} \simeq -30.54$ dB. These numbers are in good agreement with the results obtained for superconducting materials. In addition, it is worth mentioning that the scattering matrix elements between A and B calculated here with FASTHENRY for almost perfectly conducting structures are in excellent agreement with those evaluated for similar structures by means of more advanced software based on the method of moments.[68,95]

In conclusion, we study a detailed setup of two-resonator circuit QED based on a superconducting flux qubit. In this case, we prove that the geometric second-order inductance found with our three-node network approach agrees well with that obtained from numerical simulations. Moreover, we give a set of parameters (many sets can easily be found) for which the second-order inductance dominates over the first-order one.

VI. SUMMARY AND CONCLUSIONS

In this work, we first introduce the formalism of two-resonator circuit QED, i.e., the interaction between two on-chip microwave cavities and a superconducting qubit circuit. Starting from the Hamiltonian of a generic three-node network, we show that the qubit circuit mediates a geometric second-order coupling between the two resonators. For the case of strong qubit-resonator coupling, the geometric second-order interaction is a fundamental property of the system. In contrast to the geometric first-order coupling between the two resonators, the second-order one cannot arbitrarily be reduced by means of proper engineering.

With the aid of two prototypical examples, we then highlight the important role played by circuit topology in two-resonator circuit QED. Our models reveal a clear departure from a less detailed theory based on the Hamiltonian of a charge quantum circuit (e.g., a Cooper-pair box or a transmon) or a flux quantum circuit [e.g., a superconducting one or three Josephson tunnel junction(s) loop] coupled to multiple quantized microwave fields. We demonstrate that this simplified approach easily produces artifacts. We also show that our three-node network approach suffices to obtain correct results when including topological details appropriately into the definitions of the nodes.

We subsequently demonstrate the possibility of balancing a geometric coupling against a dynamic second-order one. In this way, the effective interaction between the two resonators can be controlled by means of an external bias. Based on this mechanism, we propose possible protocols for the implementation of a quantum switch and outline other advanced applications, which exploit the presence of the qubit.

Remarkably, we find that the quantum switch operation is robust against decoherence processes. In fact, we show that the qubit acts as a mere mediator of virtual excitations between the two resonators, a condition which substantially relaxes the requirements on the qubit performances.

Finally, we give detailed parameters for a specific setup of two-resonator circuit QED based on a superconducting flux qubit. We perform numerical simulations of the geometric coupling coefficients and find excellent agreement with our analytical predictions. In particular, we confirm the existence of a regime where the geometric second-order coupling dominates over the first-order one.

In conclusion, our findings show that in circuit QED, the circuit properties of the system are crucial to provide a correct picture of the problem and also constitute a major difference with respect to atomic systems. This peculiar aspect of circuit QED makes it a very rich environment for the prediction and experimental implementation of unprecedented phenomena.

ACKNOWLEDGMENTS

Financial support by the German Science Foundation through SFB 631 and the Excellence Cluster "Nanosystems Initiative Munich (NIM)" is gratefully acknowledged. This project was also partially funded by the EU EuroSQIP project, the Basque Foundation for Science (Ikerbasque), UPV-EHU Grant No. GIU07/40, and NSERC. We thank Miguel Ángel Araque Caballero, Elisabeth Hoffmann, Edwin P. Menzel, Henning Christ, Markus J. Storcz, David Zueco Láinez, Sigmund Kohler, Florian Marquardt, Jens Siewert, Martijn Wubs, William D. Oliver, Johannes B. Mejer, Yu-xi Liu, Franco Nori, and Peter Zoller for fruitful discussions.

APPENDIX A: HIGHER-ORDER CORRECTIONS TO THE CAPACITANCE AND INDUCTANCE MATRICES

In Sec. II B, we account for corrections up to second-order capacitive and inductive interactions between the elements of a three-node network. Throughout this work, we show that for a three-node network the geometric second-order coupling coefficients can dominate over the first-order ones. For this reason, in the following we can safely assume vanishing first-order coupling coefficients, $c=m=0$. Nevertheless, we notice that our results would not be qualitatively affected even in the presence of appreciable first-order couplings.

In this appendix, we demonstrate that third- and fourth-order capacitances and inductances are negligible. We start with the case of third-order corrections. There are two possible excitation pathways giving rise to third-order coupling coefficients. These pathways are between resonator A and qubit Q, A-Q-B-Q, or between resonator B and qubit Q, B-Q-A-Q. Assuming the two resonators to have identical properties, we study only the A-Q-B-Q pathway. In this case, from the knowledge of the electromagnetic energy we can derive

$$\hat{H}^{(3)}_{\mathrm{AQ}} = \hat{V}_{\mathrm{A}} C_{\mathrm{AQ}} \hat{V}_{\mathrm{Q}} + \hat{I}_{\mathrm{A}} M_{\mathrm{AQ}} \hat{I}_{\mathrm{Q}} + \hat{V}_{\mathrm{A}} C_{\mathrm{AQ}} \frac{1}{C_{\mathrm{QQ}}} C_{\mathrm{QB}} \frac{1}{C_{\mathrm{BB}}} C_{\mathrm{BQ}} \hat{V}_{\mathrm{Q}} + \hat{I}_{\mathrm{A}} M_{\mathrm{AQ}} \frac{1}{M_{\mathrm{QQ}}} M_{\mathrm{QB}} \frac{1}{M_{\mathrm{BB}}} M_{\mathrm{BQ}} \hat{I}_{\mathrm{Q}}, \tag{A1}$$

where the inverse paths Q-A and Q-B-Q-A are already included. In the equation above, resonator B is only virtually excited. In the same equation, we identify the capacitance and inductance matrix elements up to third order,

$$C_{\mathrm{AQ}}^{(3)} \equiv C_{\mathrm{AQ}}\left(1+\frac{C_{\mathrm{QB}}^2}{C_{\mathrm{QQ}}C_{\mathrm{BB}}}\right) \tag{A2}$$

and

$$M_{\mathrm{AQ}}^{(3)} \equiv M_{\mathrm{AQ}}\left(1+\frac{M_{\mathrm{QB}}^2}{M_{\mathrm{QQ}}M_{\mathrm{BB}}}\right). \tag{A3}$$

In circuit theory, it is well known that the squares of the electromagnetic coupling coefficients are[57] $C_{\mathrm{QB}}^2/C_{\mathrm{QQ}}C_{\mathrm{BB}}<1$ and $M_{\mathrm{QB}}^2/M_{\mathrm{QQ}}M_{\mathrm{BB}}<1$. This implies that the pure third-order capacitance and inductance are always smaller than the first-order ones, $C_{\mathrm{AQ}}^{(3)}-C_{\mathrm{AQ}}<C_{\mathrm{AQ}}$ and $M_{\mathrm{AQ}}^{(3)}-M_{\mathrm{AQ}}<M_{\mathrm{AQ}}$. For typical experimental parameters, we find third-order processes to be negligible, $C_{\mathrm{AQ}}^{(3)}-C_{\mathrm{AQ}}\ll C_{\mathrm{AQ}}$ and $M_{\mathrm{AQ}}^{(3)}-M_{\mathrm{AQ}}\ll M_{\mathrm{AQ}}$. For example, using the parameters given in Sec. V yields $M_{\mathrm{QB}}^2/M_{\mathrm{QQ}}M_{\mathrm{BB}}\simeq 7.88\times 10^{-4}\ll 1$.

In a similar way, the fourth-order coupling coefficients for the excitation pathways A-Q-B-Q-B and, equivalently, B-Q-A-Q-A can easily be found. In this case, it is the qubit to be only virtually excited. The capacitance and inductance matrix elements up to fourth order become

$$C_{\mathrm{AB}}^{(4)} \equiv \frac{C_{\mathrm{AQ}}C_{\mathrm{QB}}}{C_{\mathrm{QQ}}}\left(1+\frac{C_{\mathrm{QB}}^2}{C_{\mathrm{QQ}}C_{\mathrm{BB}}}\right) \tag{A4}$$

and

$$M_{\mathrm{AQ}}^{(4)} \equiv \frac{M_{\mathrm{AQ}}M_{\mathrm{QB}}}{M_{\mathrm{QQ}}}\left(1+\frac{M_{\mathrm{QB}}^2}{M_{\mathrm{QQ}}M_{\mathrm{BB}}}\right). \tag{A5}$$

When comparing the above equations to Eqs. (A2) and (A3), respectively, we find that fourth-order processes are negligible for typical experimental parameters. In the light of all these considerations, all higher-order coupling coefficients can safely be ignored within the scope of this work.

APPENDIX B: DETAILS OF THE FASTHENRY SIMULATIONS

In this appendix, we discuss the details of our FASTHENRY simulations.[92] First, we verify our hypothesis on the uniformity of the ac currents (corresponding to the magnetic fields) flowing on the resonators in the regions in Figs. 6(b) and 6(c). To this end, we derive the quantized current on one of the two resonators (e.g., A) following similar calculations as in Refs. 22 and 60,

$$\hat{I}_{ra}(z,t) \equiv i_{\mathrm{A0}}\cos\left(\frac{\pi z}{\ell_m}\right)j[\hat{a}^\dagger(t)-\hat{a}(t)], \tag{B1}$$

where z represents a coordinate along the longitudinal direction of the resonator [see Fig. 6(c)] and t is the time. In Eq. (B1), the bosonic field operators are expressed in the Heisenberg picture. We notice that Eq. (B1) is valid for the first mode of the $\lambda/2$ resonator(s) considered in our example. The contribution from the second mode is negligible for two main reasons. First, the current is characterized by a node at the flux qubit loop position chosen here. Second, the qubit-resonator detuning becomes substantially larger, hence resulting in a correspondingly reduced coupling. The contribution form higher modes can also be neglected because of the increasing detuning.

Substituting the numbers in Table I into Eq. (B1) and setting $z=\mp\ell_{\mathrm{sim}}/2$, we find that the two currents at the boundaries $\mp\ell_{\mathrm{sim}}/2$ are about $0.998i_{\mathrm{A0}}$, where i_{A0} is the maximum amplitude of the quantized current in Eq. (B1). This maximum is obtained at the position $z=0$ of the mode antinode. The main implications of current uniformity over ℓ_{sim} are explained in detail in Sec. V. In a similar way, we can also estimate the voltage contribution for the first mode at the boundaries $\mp\ell_{\mathrm{sim}}/2$. In this case, we must replace the cosine function in Eq. (B1) with a sine function, owing to the conjugation of quantized currents and voltages. The maximum vacuum voltage of, e.g., resonator A is given by $v_{\mathrm{A0}}\equiv\sqrt{\hbar\omega_{\mathrm{A}}/2C_{ra}}\simeq 0.5871$ μV for the realistic parameters in Table I. At $\mp\ell_{\mathrm{sim}}/2$, we then obtain the maximum voltages in the simulated regions, which are approximately $\mp 0.065v_{\mathrm{A0}}$. Toward the center of the simulated regions, the voltage reduces to zero because its corresponding first mode is characterized by a node. Also, higher modes do not contribute for the same detuning arguments outlined above. Therefore, we can safely neglect all capacitive couplings in our simulations.

Second, we notice that $\ell_{\mathrm{sim}}=500$ μm is chosen to be large enough compared to the lateral dimension $\ell_{q1}=200$ μm of the flux qubit loop [see Figs. 6(a)–6(c)]. This avoids errors due to fringing effects when simulating the coupling coefficients between qubit and resonators. For consistency, we have also performed several simulations assuming larger values of ℓ_{sim}, up to 1–1.5 mm (data not shown).[68] We have not found any appreciable deviation in the resulting inductances.

Third, we stress that special care has to be taken when using FASTHENRY to simulate the second-order inductances of our three-circuit network. In order to compute the inductance matrix, test currents must be applied to the involved structures at specific probing ports. However, when applying test currents to all three circuits simultaneously, only first-order inductances are calculated. This is due to the boundary conditions that must be fulfilled at the probing ports. This fact has important implications for the calculation of the mutual inductance $\tilde{m}$, which is the sum of first- and second-order mutual inductances between resonators A and B. In this case, it is crucial to apply test currents only to the two resonators but not to the qubit circuit. On the contrary, the pure first-order mutual inductance m between A and B can be simulated in two equivalent ways: Either the qubit circuit is completely removed from the network or test currents are applied to all three structures. We do not notice any difference between these two approaches. The above arguments also apply to the calculation of the renormalized self-inductances $\tilde{L}_{ra}^*$ and $\tilde{L}_{rb}^*$ of the two resonators and their pure counterparts L_{ra}^* and L_{rb}^*.

*matteo.mariantoni@wmi.badw.de
†frank.deppe@wmi.badw.de

[1] A. Wallraff, D. I. Schuster, A. Blais, L. Frunzio, R.-S. Huang, J. Majer, S. Kumar, S. M. Girvin, and R. J. Schoelkopf, Nature (London) **431**, 162 (2004).
[2] I. Chiorescu, P. Bertet, K. Semba, Y. Nakamura, C. J. P. M. Harmans, and J. E. Mooij, Nature (London) **431**, 159 (2004).
[3] J. Johansson, S. Saito, T. Meno, H. Nakano, M. Ueda, K. Semba, and H. Takayanagi, Phys. Rev. Lett. **96**, 127006 (2006).
[4] R. J. Schoelkopf and S. M. Girvin, Nature (London) **451**, 664 (2008).
[5] M. A. Sillanpää, J. I. Park, and R. W. Simmonds, Nature (London) **449**, 438 (2007).
[6] J. Majer, J. M. Chow, J. M. Gambetta, J. Koch, B. R. Johnson, J. A. Schreier, L. Frunzio, D. I. Schuster, A. A. Houck, A. Wallraff, A. Blais, M. H. Devoret, S. M. Girvin, and R. J. Schoelkopf, Nature (London) **449**, 443 (2007).
[7] A. A. Houck, D. I. Schuster, J. M. Gambetta, J. A. Schreier, B. R. Johnson, J. M. Chow, L. Frunzio, J. Majer, M. H. Devoret, S. M. Girvin, and R. J. Schoelkopf, Nature (London) **449**, 328 (2007).
[8] M. Hofheinz, E. M. Weig, M. Ansmann, R. C. Bialczak, E. Lucero, M. Neeley, A. D. O'Connell, H. Wang, J. M. Martinis, and A. N. Cleland, Nature (London) **454**, 310 (2008).
[9] O. Astafiev, K. Inomata, A. O. Niskanen, T. Yamamoto, Yu. A. Pashkin, Y. Nakamura, and J. S. Tsai, Nature (London) **449**, 588 (2007).
[10] J. M. Fink, M. Göppl, M. Baur, R. Bianchetti, P. J. Leek, A. Blais, and A. Wallraff, Nature (London) **454**, 315 (2008).
[11] L. S. Bishop, J. M. Chow, J. Koch, A. A. Houck, M. H. Devoret, E. Thuneberg, S. M. Girvin, and R. J. Schoelkopf, arXiv:0807.2882 (unpublished).
[12] F. Deppe, M. Mariantoni, E. P. Menzel, A. Marx, S. Saito, K. Kakuyanagi, H. Tanaka, T. Meno, K. Semba, H. Takayanagi, E. Solano, and R. Gross, Nat. Phys. **4**, 686 (2008).
[13] A. Palacios-Laloy, F. Nguyen, F. Mallet, P. Bertet, D. Vion, and D. Esteve, J. Low Temp. Phys. **151**, 1034 (2008).
[14] M. Sandberg, C. M. Wilson, F. Persson, G. Johansson, V. Shumeiko, T. Duty, and P. Delsing, Appl. Phys. Lett. **92**, 203501 (2008).
[15] H. Mabuchi and A. C. Doherty, Science **298**, 1372 (2002).
[16] S. Haroche and J.-M. Raimond, *Exploring the Quantum* (Oxford University Press, New York, 2006).
[17] H. Walther, B. T. H. Varcoe, B. G. Englert, and T. Becker, Rep. Prog. Phys. **69**, 1325 (2006).
[18] M. A. Nielsen and I. L. Chuang, *Quantum Computation and Quantum Information* (Cambridge University Press, Cambridge, England, 2000).
[19] A. Blais, J. Gambetta, A. Wallraff, D. I. Schuster, S. M. Girvin, M. H. Devoret, and R. J. Schoelkopf, Phys. Rev. A **75**, 032329 (2007).
[20] F. Helmer, M. Mariantoni, A. G. Fowler, J. von Delft, E. Solano, and F. Marquardt, arXiv:0706.3625 (unpublished).
[21] M. J. Storcz, M. Mariantoni, H. Christ, A. Emmert, A. Marx, W. D. Oliver, R. Gross, F. K. Wilhelm, and E. Solano, arXiv:cond-mat/0612226 (unpublished).
[22] A. Blais, R.-S. Huang, A. Wallraff, S. M. Girvin, and R. J. Schoelkopf, Phys. Rev. A **69**, 062320 (2004).
[23] M. Mariantoni and F. Deppe (unpublished).
[24] D. I. Schuster, A. A. Houck, J. A. Schreier, A. Wallraff, J. M. Gambetta, A. Blais, L. Frunzio, J. Majer, B. Johnson, M. H. Devoret, S. M. Girvin, and R. J. Schoelkopf, Nature (London) **445**, 515 (2007).
[25] R. H. Koch, G. A. Keefe, F. P. Milliken, J. R. Rozen, C. C. Tsuei, J. R. Kirtley, and D. P. DiVincenzo, Phys. Rev. Lett. **96**, 127001 (2006).
[26] Yu. Makhlin, G. Schön, and A. Shnirman, Rev. Mod. Phys. **73**, 357 (2001).
[27] M. H. Devoret, A. Wallraff, and J. M. Martinis, arXiv:cond-mat/0411174 (unpublished).
[28] J. Q. You and F. Nori, Phys. Today **58**(11), 42 (2005).
[29] G. Wendin and V. Shumeiko, in *Handbook of Theoretical and Computational Nanotechnology*, edited by M. Rieth and W. Schommers (American Scientific, Los Angeles, 2006), Vol. 3, pp. 223–309; see also arXiv:cond-mat/0508729 (unpublished).
[30] A. Rauschenbeutel, P. Bertet, S. Osnaghi, G. Nogues, M. Brune, J. M. Raimond, and S. Haroche, Phys. Rev. A **64**, 050301(R) (2001).
[31] O. Buisson and F. W. J. Hekking, in *Macroscopic Quantum Coherence and Computing*, edited by D. V. Averin, B. Ruggiero, and P. Silvestrini (Kluwer, New York, 2001), pp. 137–146.
[32] C. P. Yang, S.-I Chu, and S. Han, Phys. Rev. A **67**, 042311 (2003).
[33] F. Plastina and G. Falci, Phys. Rev. B **67**, 224514 (2003).
[34] J. Q. You and F. Nori, Phys. Rev. B **68**, 064509 (2003).
[35] A. Messina, S. Maniscalco, and A. Napoli, J. Mod. Opt. **50**, 1 (2003).
[36] C. P. Sun, L. F. Wei, Yu Xi Liu, and F. Nori, Phys. Rev. A **73**, 022318 (2006).
[37] F. L. Semião, K. Furuya, and G. J. Milburn, arXiv:0808.0743 (unpublished).
[38] A. Blais, J. M. Gambetta, C. Cheung, A. Wallraff, D. I. Schuster, S. M. Girvin, and R. J. Schoelkopf, http://meetings.aps.org/link/BAPS.2007.MAR.H33.5
[39] M. Wubs, S. Kohler, and P. Hänggi, Physica E (Amsterdam) **40**, 187 (2007).
[40] F. Helmer, M. Mariantoni, E. Solano, and F. Marquardt, arXiv:0712.1908 (unpublished).
[41] P. Xue, B. C. Sanders, A. Blais, and K. Lalumiere, arXiv:0802.2750 (unpublished).
[42] L. Zhou, Z. R. Gong, Yu-xi Liu, C. P. Sun, and F. Nori, arXiv:0802.4204 (unpublished).
[43] L. Davidovich, A. Maali, M. Brune, J. M. Raimond, and S. Haroche, Phys. Rev. Lett. **71**, 2360 (1993).
[44] D. V. Averin and C. Bruder, Phys. Rev. Lett. **91**, 057003 (2003).
[45] E. Il'ichev, N. Oukhanski, A. Izmalkov, T. Wagner, M. Grajcar, H. G. Meyer, A. Y. Smirnov, A. Maassen van den Brink, M. H. S. Amin, and A. M. Zagoskin, Phys. Rev. Lett. **91**, 097906 (2003).
[46] B. L. T. Plourde, J. Zhang, K. B. Whaley, F. K. Wilhelm, T. L. Robertson, T. Hime, S. Linzen, P. A. Reichardt, C.-E. Wu, and J. Clarke, Phys. Rev. B **70**, 140501(R) (2004).
[47] A. Lupaşcu, C. J. M. Verwijs, R. N. Schouten, C. J. P. M. Harmans, and J. E. Mooij, Phys. Rev. Lett. **93**, 177006 (2004).
[48] M. A. Sillanpää, T. Lehtinen, A. Paila, Yu. Makhlin, L. Roschier, and P. J. Hakonen, Phys. Rev. Lett. **95**, 206806 (2005).
[49] T. Duty, G. Johansson, K. Bladh, D. Gunnarsson, C. Wilson, and P. Delsing, Phys. Rev. Lett. **95**, 206807 (2005).
[50] G. Johansson, L. Tornberg, V. S. Shumeiko, and G. Wendin, J. Phys.: Condens. Matter **18**, S901 (2006).

[51] J. Könemann, H. Zangerle, B. Mackrodt, R. Dolata, and A. B. Zorin, Phys. Rev. B **76**, 134507 (2007).
[52] B. Yurke and J. S. Denker, Phys. Rev. A **29**, 1419 (1984).
[53] G. Burkard, R. H. Koch, and D. P. DiVincenzo, Phys. Rev. B **69**, 064503 (2004).
[54] G. Burkard, Phys. Rev. B **71**, 144511 (2005).
[55] G. Burkard, in *Handbook of Theoretical and Computational Nanotechnology*, edited by M. Rieth and W. Schommers (American Scientific, New York, 2005); see arXiv:cond-mat/0409626 (unpublished).
[56] G. Wendin and V. S. Shumeiko, Low Temp. Phys. **33**, 724 (2007).
[57] L. O. Chua, C. A. Desoer, and E. S. Kuh, *Linear and Nonlinear Circuits* (McGraw-Hill, New York, 1987).
[58] F. Deppe, M. Mariantoni, E. P. Menzel, S. Saito, K. Kakuyanagi, H. Tanaka, T. Meno, K. Semba, H. Takayanagi, and R. Gross, Phys. Rev. B **76**, 214503 (2007).
[59] In two of our previous works (Refs. 20 and 21), we studied charge qubits in multiresonator systems. In that case, we performed numerical simulations to study the geometric first-order capacitance between two resonators [in a configuration similar to that of Fig. 1(e)]. We found a scattering matrix element $S_{ab} \simeq -50$ dB at approximately 4 GHz, which gives $C_{\mathrm{AB}}=c=3\times10^{-3}C_{\mathrm{BB}}$. Assuming $C_{\mathrm{AQ}}\simeq C_{\mathrm{QB}}$, we can easily compare c to the second-order cross capacitance between A and B and obtain $c/(C_{\mathrm{AQ}}^2/C_{\mathrm{QQ}})\simeq 0.9$. For these calculations, we use $C_{\mathrm{BB}}\simeq 2.2$ pF, $C_{\mathrm{AQ}}\simeq 22$ fF, and $C_{\mathrm{QQ}}\simeq 67$ fF from Ref. 6. In particular, we find $c\simeq 7$ fF and $C_{\mathrm{AQ}}C_{\mathrm{QB}}/C_{\mathrm{QQ}}\simeq 7.5$ fF. In this case, an example of third-order cross capacitance is $C_{\mathrm{AQ}}C_{\mathrm{QB}}C_{\mathrm{BQ}}/C_{\mathrm{QQ}}C_{\mathrm{BB}}\simeq 76$ aF, which is negligible.
[60] M. Mariantoni, M. J. Storcz, F. K. Wilhelm, W. D. Oliver, A. Emmert, A. Marx, R. Gross, H. Christ, and E. Solano, arXiv:cond-mat/0509737 (unpublished).
[61] J. Koch, T. M. Yu, J. Gambetta, A. A. Houck, D. I. Schuster, J. Majer, A. Blais, M. H. Devoret, S. M. Girvin, and R. J. Schoelkopf, Phys. Rev. A **76**, 042319 (2007).
[62] J. A. Schreier, A. A. Houck, J. Koch, D. I. Schuster, B. R. Johnson, J. M. Chow, J. M. Gambetta, J. Majer, L. Frunzio, M. H. Devoret, S. M. Girvin, and R. J. Schoelkopf, Phys. Rev. B **77**, 180502(R) (2008).
[63] A. A. Houck, J. A. Schreier, B. R. Johnson, J. M. Chow, J. Koch, J. M. Gambetta, D. I. Schuster, L. Frunzio, M. H. Devoret, S. M. Girvin, and R. J. Schoelkopf, Phys. Rev. Lett. **101**, 080502 (2008).
[64] T. Lindström, C. H. Webster, J. E. Healey, M. S. Colclough, C. M. Muirhead, and A. Ya. Tzalenchuk, J. Phys.: Conf. Ser. **97**, 012319 (2008).
[65] In the definition of self-capacitance, we neglect the capacitance of the island itself because it is small compared to the other capacitances, $C_{\mathrm{isl}}\ll\min\{C_{ga},2C_J,C_{gb}\}$.
[66] The remaining two interaction terms, when quantizing the ac excitations, result in a displacement-type operator (Ref. 22), which act on the two resonators' coordinates. These operators reduce to zero right at the charge degeneracy point (i.e., for $n_g^{\mathrm{dc}}=1/2$). In general, these terms are small and can thus be neglected (Ref. 22).
[67] T. P. Orlando, J. E. Mooij, L. Tian, C. H. van der Wal, L. S. Levitov, S. Lloyd, and J. J. Mazo, Phys. Rev. B **60**, 15398 (1999).
[68] M. Mariantoni (unpublished).
[69] C. Wildfeuer and D. H. Schiller, Phys. Rev. A **67**, 053801 (2003).
[70] T. Niemczyk (private communication).
[71] Yu-xi Liu, L. F. Wei, and F. Nori, Europhys. Lett. **67**, 941 (2004).
[72] N. Kiesel, C. Schmid, G. Tóth, E. Solano, and H. Weinfurter, Phys. Rev. Lett. **98**, 063604 (2007).
[73] A. Wallraff, D. I. Schuster, A. Blais, L. Frunzio, J. Majer, M. H. Devoret, S. M. Girvin, and R. J. Schoelkopf, Phys. Rev. Lett. **95**, 060501 (2005).
[74] L. F. Wei, Yu-Xi Liu, and F. Nori, Phys. Rev. Lett. **96**, 246803 (2006).
[75] Yu-xi Liu, L. F. Wei, and F. Nori, Phys. Rev. A **71**, 063820 (2005).
[76] E. Solano, R. L. de Matos Filho, and N. Zagury, Phys. Rev. Lett. **87**, 060402 (2001).
[77] E. Solano, R. L. de Matos Filho, and N. Zagury, J. Opt. B: Quantum Semiclassical Opt. **4**, S324 (2002).
[78] M. Steffen, M. Ansmann, R. McDermott, N. Katz, R. C. Bialczak, E. Lucero, M. Neeley, E. M. Weig, A. N. Cleland, and J. M. Martinis, Phys. Rev. Lett. **97**, 050502 (2006).
[79] P. Bertet, I. Chiorescu, G. Burkard, K. Semba, C. J. P. M. Harmans, D. P. DiVincenzo, and J. E. Mooij, Phys. Rev. Lett. **95**, 257002 (2005).
[80] F. Yoshihara, K. Harrabi, A. O. Niskanen, Y. Nakamura, and J. S. Tsai, Phys. Rev. Lett. **97**, 167001 (2006).
[81] K. Kakuyanagi, T. Meno, S. Saito, H. Nakano, K. Semba, H. Takayanagi, F. Deppe, and A. Shnirman, Phys. Rev. Lett. **98**, 047004 (2007).
[82] At the qubit degeneracy point, the scenario can be quite different and energy relaxation can become the dominating source of decoherence. However, qubit energy relaxation rates are typically $\lesssim$10 MHz in this situation. Thus, a reasonable operating time for the quantum switch is guaranteed.
[83] S. Saito, T. Meno, M. Ueda, H. Tanaka, K. Semba, and H. Takayanagi, Phys. Rev. Lett. **96**, 107001 (2006).
[84] J. Hauss, A. Fedorov, C. Hutter, A. Shnirman, and G. Schön, Phys. Rev. Lett. **100**, 037003 (2008).
[85] L. Frunzio, A. Wallraff, D. Schuster, J. Majer, and R. Schoelkopf, IEEE Trans. Appl. Supercond. **15**, 860 (2005).
[86] J. M. Martinis, K. B. Cooper, R. McDermott, M. Steffen, M. Ansmann, K. D. Osborn, K. Cicak, S. Oh, D. P. Pappas, R. W. Simmonds, and C. C. Yu, Phys. Rev. Lett. **95**, 210503 (2005).
[87] A. D. O'Connell, M. Ansmann, R. C. Bialczak, M. Hofheinz, N. Katz, E. Lucero, C. McKenney, M. Neeley, H. Wang, E. M. Weig, A. N. Cleland, and J. M. Martinis, Appl. Phys. Lett. **92**, 112903 (2008).
[88] J. Gao, M. Daal, A. Vayonakis, S. Kumar, J. Zmuidzinas, B. Sadoulet, B. A. Mazin, P. K. Day, and H. G. Leduc, Appl. Phys. Lett. **92**, 152505 (2008).
[89] J. Gao, M. Daal, J. M. Martinis, A. Vayonakis, J. Zmuidzinas, B. Sadoulet, B. A. Mazin, P. K. Day, and H. G. Leduc, Appl. Phys. Lett. **92**, 212504 (2008).
[90] R. Barends, H. L. Hortensius, T. Zijlstra, J. J. A. Baselmans, S. J. C. Yates, J. R. Gao, and T. M. Klapwijk, Appl. Phys. Lett. **92**, 223502 (2008).
[91] However, in order to avoid unwanted reflections, all on-chip transmission lines connected to the resonators via the input and output capacitors have to be properly engineered to be 50 Ω matched.

[92] FASTHENRY, Inductance Analysis Program, RLE Computational Prototyping Group, Boston; M. Kamon, M. J. Tsuk, and J. K. White, IEEE Trans. Microwave Theory Tech. **42**, 1750 (1994); see also http://www.fastfieldsolvers.com and and http://www.wrcad.com/freestuff.html

[93] B. L. T. Plourde, T. L. Robertson, P. A. Reichardt, T. Hime, S. Linzen, C.-E. Wu, and J. Clarke, Phys. Rev. B **72**, 060506(R) (2005).

[94] Obviously, this does not mean that sharp edges of the microwave on-chip structures are needed (which would imply unwanted radiation effects). It only means that the lines of the two resonators have to rapidly depart from each other.

[95] R. E. Collin, *Foundations for Microwave Engineering*, 2nd ed. (Wiley, New Jersey, 2000).

[96] D. M. Pozar, *Microwave Engineering*, 3rd ed. (Wiley, New Jersey, 2005).

[97] In all our calculations and simulations, for the permittivity of vacuum we use the standard value provided by the National Institute of Standards and Technology (NIST), retaining all given decimal digits. The same applies for all other fundamental physical constants, which can be found at http://physics.nist.gov/cuu/Constants/